Energetics of Lipid Bilayer Fusion by the GTPase Atlastin

by

James Winsor

Department of Biological Sciences
Carnegie Mellon University
Pittsburgh, PA 15213

April 30th, 2018

Thesis Advisor: Dr. Tina H. Lee, PhD

Contents

Introduction

Fusion of lipid bilayers underpin a huge variety of processes within a Eukaryotic cell, from protein trafficking to endocytosis and organelle maintenance. Eukaryotic cells are defined by their separate internal compartments that allow for unique chemistry and biology to occur, and lipid bilayers separate each compartment from another. The inherent stability and resistance of lipid bilayers to spontaneous fusion allows these unique compartments to remain separate, however it also presents a problem for the cell. In order for cargos to transfer from one compartment to another they must pass this stable lipid bilayer. One method of doing this is vesicular trafficking where a cargo is placed in a vesicle that buds off of its original compartment and is taken to the target compartment. The vesicle must then fuse with the target membrane to release its cargo. While the fusion of two lipid bilayers is energetically favorable, there is a large energy barrier that prevents spontaneous fusion. This energy is a result of the hydrophobic effect stabilizing the hydrophobic tail of phospholipids away from the aqueous environment as well as Van der Walls and hydration forces promoting head group interactions with the aqueous environment (Donaldson et al., 2015). In order to initiate fusion a highly unfavorable intermediate where the hydrophobic tail of lipid molecules must be removed from their preferred hydrophobic environment and into an aqueous one (Ryham, Klotz, Yao, & Cohen, 2016). In order to overcome this barrier cells utilize fusion catalysts that act both to lower the energy barrier and provide the remaining energy for bilayer fusion.

Vesicular Trafficking

As a critical part of the secretory pathway the SNARE proteins may be the most well studied examples of a fusion catalyst. The SNARE proteins are responsible for fusion during vesicular trafficking within Eukaryotic cells and underpin diverse processes such as synaptic vesicle fusion with the plasma membrane, ER-Golgi trafficking, and Endosome-Lysosome fusion. A large number of SNARE proteins

have been identified, allowing membrane specificity, but the mechanism for all known SNAREs is very similar (McNew et al., 2000). SNARE proteins are helical proteins embedded in the membranes by either a transmembrane region or a post-translational modification such as palmitoylation (Vogel & Roche, 1999). One SNARE protein on the vesicle to be fused, known as the v-SNARE, forms a *trans* complex with a snare bundle, typically consisting of 2-3 subunits, on the target membrane, known as the t-SNARE. This complex forms a highly favorable 4-helix bundle that is capable of drawing membranes into close apposition and releasing the energy required for membrane fusion (Weber et al., 1998). Measurements of the force and energy a single SNARE bundle is capable of utilizing during "zippering" has shown that fusion likely requires several, approximately 5 to 10, of these complexes working in concert to efficiently catalyze fusion (Karatekin et al., 2010). Following fusion the 4-helix bundle, now in *cis*, of the SNARE proteins must be unwound for reuse in future fusion reactions.

This unwinding of the SNARE complex is mediated by the ATPase NSF and SNAP proteins. The exact mechanism of this disassembly has remained elusive, however, it is clear that the hydrolysis by NSF is utilized to force conformational changes of the SNARE complex that promote disassembly (Zhao et al., 2015). Following this disassembly the SNARE proteins are recycled to their initial compartment for reuse.

Viral Fusion

The critical step in a viral infection is the release of viral genetic material into the host cell. As many viruses are enveloped by a lipid bilayer this necessitates fusion proteins to allow the contents of the virus to enter the cell. A number of different classes of viral fusion proteins exist, but all share a few commonalities with perhaps the best studied member, Hemagglutinin (HA), used during entry by the influenza virus. Following uptake into an endosomal compartment and trafficking towards the lysosome the HA protein extends from the viral membrane and inserts into the endosome's bilayer forming a

trans complex with insertions in both bilayers. These *trans* complexes then form trimers that undergo a series of favorable conformational shifts that initiate membrane fusion by releasing energy and drawing the membranes close together, similar to the SNARE proteins leading to a *cis* complex on the final fused membrane (Blijleven, Boonstra, Onck, van der Giessen, & van Oijen, 2016). As with the SNARE proteins multiple complexes are necessary to release the energy required for fusion (Ivanovic, Choi, Whelan, van Oijen, & Harrison, 2013). No subsequent recycling of this final *cis* complex is observed as only a single round of fusion is necessary for viral entry.

Homotypic membrane fusion

Both above examples show the fusion of bilayers that form separate compartments, however, homotypic fusion also occurs commonly as a part of organelle maintenance. Both the endoplasmic reticuluum (ER) and mitochondria are highly dynamic organelles that regularly undergo homotypic fusion events as a part of their continuous restructuring. It has recently become clear that the fusion machinery for these organelles occurs through a mechanism unrelated to the SNARE proteins.

The atlastin family of proteins, responsible for ER fusion, along with the related mitofusins responsible for mitochondrial fusion, share some traits with other fusion proteins. An initial *trans* complex spanning the bilayers to be fused undergoes a large conformational shift, termed crossover, leading to fusion. However, as a GTPase, atlastin has an additional source of energy beyond the favorable conformational shifts available to other fusion proteins and could couple the breakage of a high energy phosphate bond directly to membrane fusion. In fact, recent advances in understanding the mechanism of atlastin mediated fusion has strongly hinted that GTP hydrolysis is playing a role directly coupled to bilayer fusion.

Energetics of Atlastin

Identification of atlastin as the primary source of homotypic membrane fusion within the ER came when atlastin was shown to be capable of fusing vesicles in vitro absent any additional proteins (Orso et al., 2009). This fusion activity proceeded in a GTP dependent manner, and somewhat surprisingly, appeared to require nucleotide hydrolysis. GTPγS, a non-hydrolysable GTP analog, proved incapable of inducing fusion under the same conditions as GTP implying a requirement for nucleotide hydrolysis upstream or concurrent with fusion. Following up on this finding crystal structures of human atlastin-1 were solved revealing three distinct conformations and allowing a better understanding of the domain structure of these proteins as well as how they may change conformations during the fusion reaction (Bian et al., 2011; Byrnes et al., 2013).

The first crystal structure showed the G-domain head group dimerized with a connecting three helix bundle extended in opposite directions by each monomer. These bundles ended where the protein had been truncated just prior to the transmembrane domains of the protein implying that this dimer was likely an early *trans* dimer forming to span two lipid bilayers (Bian et al., 2011). The other two crystal structures are similar, with the three helix bundles undergoing a large conformational change where they dimerize with each other and cross over to be under the partner's G-domain (Bian et al., 2011; Byrnes et al., 2013). The major difference between the two is one conformation has much more extensive contacts between the dimer partners. Based on where the transmembrane regions would be if not truncated in these structures it is difficult to envision how either the tight or loose crossover dimer could be in separate membranes and likely represent post fusion conformations. Beyond the transmembrane region an additional C-terminal domain is present that was later shown to be an amphipathic helix. The large conformational change observed in the soluble domain (G-domain and three helix bundles) was reminiscent of the sort of conformational changes observed in other fusion proteins. However, this immediately raises a question, if in the process of fusion, atlastin undergoes a

large and presumably favorable conformational change like other fusion proteins, why is GTP hydrolysis required for atlastin mediated fusion?

Answers to what role GTP hydrolysis may be playing came with more detailed biochemical studies of the atlastin soluble domain. Early studies showed that soluble atlastin was capable of dimerizing with either GTP, non-hydrolysable GMPPNP, or the transition state analog GDP▪AlF_4, but did not dimerize in the presence of GDP (Bian et al., 2011; Byrnes & Sondermann, 2011; Morin-Leisk et al., 2011; Saini, Liu, Zhang, & Lee, 2014). While GTP, GMPPNP, and GDP▪AlF_4 all readily formed dimers, an analysis of the rates of atlastin dimerization in the presence of each nucleotide showed a possible role for GTP hydrolysis (Byrnes et al., 2013). Under similar conditions, GMPPNP and GDP▪AlF_4 based dimerization proceeded relatively slowly, taking at least several minutes to complete dimerization, while GTP based dimerization reached completion within a second or two. This implies a situation where GTP hydrolysis greatly stimulates atlastin's ability to dimerize. Further evidence for this claim came with EM images of in vitro vesicles containing full length atlastin. These vesicles showed clustering with the formation of long "zippers" between vesicles in the presence of GTP, while GMPPNP showed no dimerization between vesicles (Saini et al., 2014). Together this implies a model of hydrolysis where GTP initially binds, and is then quickly hydrolyzed into GDP▪Pi by the monomer which utilizes that energy to dimerize. The slow rate of dimerization by the transition state GDP▪AlF_4 implies that the actual energy of hydrolysis is needed for dimerization, rather than simply GDP▪Pi production as a dimerization capable intermediate (Byrnes et al., 2013). Further evidence for this model comes from recent work suggesting that atlastin hydrolysis is extremely rapid, and precedes dimerization (O'Donnell et al., 2017).

Membrane Disruption

While rates of dimerization and the possible role of hydrolysis were being elucidated other groups were looking at what role the amphipathic helix in the C-terminal region of atlastin may be playing.

Alignments across species showed that all atlastins maintained the amphipathic nature of the C-terminal helix suggesting an important role that it may be playing (Liu et al., 2012). Work on the SNARE proteins has shown that accessory proteins, such as Munc18, can play a role to disrupt the normally stable structure of the lipid bilayers, lowering the energy barrier that the SNARE proteins must overcome to fuse membranes (Wickner & Rizo, 2017). This is done through amphipathic structures of the protein that insert into the bilayer disrupting its structure. Transferring this knowledge to the atlastin fusion mechanism suggests that the amphipathic tail's purpose may be to disrupt bilayer cohesion and ease the ability of atlastin to fuse membranes. Mutational studies on atlastin suggest that the tail is acting in largely that manner. *In vitro,* mutations to the hydrophobic side of the amphipathic helix predicted to prevent insertion into the bilayer act as a strong inhibitor to fusion (Faust et al., 2015). *In vivo* fusion seems somewhat more permissive, requiring multiple mutations to inhibit fusion. Somewhat surprisingly, the same studies showed that atlastin's C-terminal tail may be acting through a more complex mechanism than simple bilayer disruption. Other amphipathic helixes known to disrupt bilayers were not capable of substituting for atlastin's tail, while atlastin's tail did not appear to disrupt the bilayer enough to cause content leakage unlike previously studied bilayer disrupting peptides (Liu et al., 2012). However, the exact reasons for this have not been further elucidated and remain a mystery.

Model

Taken together the evidence points to a model where GTP hydrolysis is initially used to stimulate *trans* atlastin dimerization across two lipid bilayers. Atlastin then undergoes crossover to draw the membranes together. Together with the disruption to the lipid bilayer by the amphipathic helix lowering the energy requirement this conformational shift releases enough energy to initiate bilayer fusion. Following this atlastin dimers disassemble, likely through the release of Pi, allowing them to be reused for additional rounds of fusion. However, this model implies that the actual crossover dimer likely releases relatively little energy during crossover as disassembly must occur without energy input

from GTP hydrolysis. This is possible, however, it requires either the amphipathic atlastin tail acting as a much more effective bilayer disruptor than other fusion accessory proteins, or for atlastin to act in a highly cooperative manner with many atlastin dimers acting in concert to together initiate bilayer fusion. Both of these models for fusion would predict a relatively unstable dimer compared to other fusion proteins to allow for dimer disassembly to actually occur, something not seen in other fusion proteins.

Goals

In this thesis, I sought to unravel this apparently unusual energetic landscape of atlastin based fusion. As such, an important first step to understand the atlastin fusion mechanism is looking at the energy contribution of an atlastin dimer to fusion. Somewhat surprisingly, and contrary to prediction, when we probed the atlastin dimer we saw that the wild type crossover dimer was extremely stable, with no observable disassembly occurring within two hours. Further probing of this dimer showed that as crossover favorability was reduced through targeted mutagenesis the stability of the dimer was reduced in kind, and along with it fusion activity was reduced, and eventually abolished. This result seemed to indicate a fundamental problem with previous models, such a stable dimer should not be capable of being disassembled without energy input, and yet the only other energy input, nucleotide hydrolysis, appeared required for dimerization.

Further probing of the atlastin mechanism shows that, contrary to other reports, hydrolysis acts late during atlastin fusion, and in fact, only appears necessary for dimer disassembly. The apparent defect in atlastin dimerization seen in non-hydrolysable analogs is, in fact, an artifact of the analogs acting as a poor GTP analog in this system. Unlike analogs, GTP triggers a unique and rapid conformational shift upon nucleotide binding, preceding dimerization. This unique conformational shift allows the rapid dimerization absent in other GTP analogs. Only after dimerization and crossover have occurred is GTP hydrolyzed. GTP hydrolysis and Pi release occur nearly simultaneously just prior to dimer disassembly.

As a result, a model of atlastin based fusion is formed that shows remarkable similarity to other fusion mechanisms where conformational shifts drive bilayer mixing through the release of energy, and then nucleotide hydrolysis is utilized to disassemble the post-fusion complex to allow for subsequent rounds of fusion.

References

Bian, X., Klemm, R. W., Liu, T. Y., Zhang, M., Sun, S., Sui, X., … Hu, J. (2011). Structures of the atlastin GTPase provide insight into homotypic fusion of endoplasmic reticulum membranes. *Proceedings of the National Academy of Sciences of the United States of America*, *108*(10), 3976–81. doi:10.1073/pnas.1101643108

Blijleven, J. S., Boonstra, S., Onck, P. R., van der Giessen, E., & van Oijen, A. M. (2016). Mechanisms of influenza viral membrane fusion. *Seminars in Cell and Developmental Biology*, *60*, 78–88. doi:10.1016/j.semcdb.2016.07.007

Byrnes, L. J., Singh, A., Szeto, K., Benvin, N. M., O'Donnell, J. P., Zipfel, W. R., & Sondermann, H. (2013). Structural basis for conformational switching and GTP loading of the large G protein atlastin. *The EMBO Journal*, *32*(3), 369–84. doi:10.1038/emboj.2012.353

Byrnes, L. J., & Sondermann, H. (2011). Structural basis for the nucleotide-dependent dimerization of the large G protein atlastin-1/SPG3A. *Proceedings of the National Academy of Sciences of the United States of America*, *108*(6), 2216–2221. doi:10.1073/pnas.1012792108

Donaldson, S. H., Royne, A., Kristiansen, K., Rapp, M. V., Das, S., Gebbie, M. A., … Israelachvili, J. (2015). Developing a general interaction potential for hydrophobic and hydrophilic interactions. *Langmuir*, *31*(7), 2051–2064. doi:10.1021/la502115g

Faust, J. E., Desai, T., Verma, a., Ulengin, I., Sun, T.-L., Moss, T. J., … McNew, J. a. (2015). The Atlastin C-terminal Tail is an Amphipathic Helix that Perturbs Bilayer Structure during Endoplasmic Reticulum Homotypic Fusion. *Journal of Biological Chemistry*. doi:10.1074/jbc.M114.601823

Ivanovic, T., Choi, J. L., Whelan, S. P., van Oijen, A. M., & Harrison, S. C. (2013). Influenza-virus membrane fusion by cooperative fold-back of stochastically induced hemagglutinin intermediates.

eLife, *2013*(2), 1–20. doi:10.7554/eLife.00333

Karatekin, E., Di Giovanni, J., Iborra, C., Coleman, J., O'Shaughnessy, B., Seagar, M., & Rothman, J. E. (2010). A fast, single-vesicle fusion assay mimics physiological SNARE requirements. *Proceedings of the National Academy of Sciences*, *107*(8), 3517–3521. doi:10.1073/pnas.0914723107

Liu, T. Y., Bian, X., Sun, S., Hu, X., Klemm, R. W., Prinz, W. a, … Hu, J. (2012). Lipid interaction of the C terminus and association of the transmembrane segments facilitate atlastin-mediated homotypic endoplasmic reticulum fusion. *Proceedings of the National Academy of Sciences of the United States of America*, *109*(32), E2146–54. doi:10.1073/pnas.1208385109

McNew, J. A., Parlatl, F., Fukuda, R., Johnston, R. J., Paz, K., Paumet, F., … Rothman, J. E. (2000). Compartmental specificity of cellular membrane fusion encoded in SNARE proteins. *Nature*, *407*(6801), 153–159. doi:10.1038/35025000

Morin-Leisk, J., Saini, S. G., Meng, X., Makhov, A. M., Zhang, P., & Lee, T. H. (2011). An intramolecular salt bridge drives the soluble domain of GTP-bound atlastin into the postfusion conformation. *The Journal of Cell Biology*, *195*(4), 605–15. doi:10.1083/jcb.201105006

O'Donnell, J. P., Cooley, R. B., Kelly, C. M., Miller, K., Andersen, O. S., Rusinova, R., & Sondermann, H. (2017). Timing and Reset Mechanism of GTP Hydrolysis-Driven Conformational Changes of Atlastin. *Structure*, *25*(7), 997–1010.e4. doi:10.1016/j.str.2017.05.007

Orso, G., Pendin, D., Liu, S., Tosetto, J., Moss, T. J., Faust, J. E., … Daga, A. (2009). Homotypic fusion of ER membranes requires the dynamin-like GTPase atlastin. *Nature*, *460*(7258), 978–983. doi:10.1038/nature08886

Ryham, R. J., Klotz, T. S., Yao, L., & Cohen, F. S. (2016). Calculating Transition Energy Barriers and Characterizing Activation States for Steps of Fusion. *Biophysical Journal*, *110*(5), 1110–1124.

doi:10.1016/j.bpj.2016.01.013

Saini, S. G., Liu, C., Zhang, P., & Lee, T. H. (2014). Membrane tethering by the atlastin GTPase depends on GTP hydrolysis but not on forming the crossover configuration. *Molecular Biology of the Cell*. doi:10.1091/mbc.E14-08-1284

Vogel, K., & Roche, P. A. (1999). SNAP-23 and SNAP-25 are palmitoylated in vivo. *Biochemical and Biophysical Research Communications*, *258*(2), 407–410. doi:10.1006/bbrc.1999.0652

Weber, T., Zemelman, B. V., McNew, J. A., Westermann, B., Gmachl, M., Parlati, F., … Rothman, J. E. (1998). SNAREpins: Minimal machinery for membrane fusion. *Cell*, *92*(6), 759–772. doi:10.1016/S0092-8674(00)81404-X

Wickner, W., & Rizo, J. (2017). A cascade of multiple proteins and lipids catalyzes membrane fusion, *28*, 707–711. doi:10.1091/mbc.E16-07-0517

Zhao, M., Wu, S., Zhou, Q., Vivona, S., Cipriano, D. J., Cheng, Y., & Brunger, A. T. (2015). Mechanistic insights into the recycling machine of the SNARE complex. *Nature*, *518*(7537), 61–67. doi:10.1038/nature14148

The crossover conformational shift of the GTPase atlastin provides the energy driving ER fusion

James Winsor, David D. Hackney and Tina H. Lee*

Department of Biological Sciences
Carnegie Mellon University
Pittsburgh, PA 15213

This manuscript appears as an article in the Journal of Cell Biology and is reprinted here

Winsor, J., D.D. Hackney, and T.H. Lee. 2017. The crossover conformational shift of the GTPase atlastin provides the energy driving ER fusion. *J Cell Biol*. 216:1321-1335.

Abstract

The homotypic fusion of endoplasmic reticulum (ER) membranes is catalyzed by the atlastin GTPase. The mechanism involves *trans* dimerization between GTPase heads and a favorable crossover conformational shift, catalyzed by GTP hydrolysis, that converts the dimer from a 'pre-fusion' to 'post-fusion' state. However, whether crossover formation actually energizes fusion remains unclear, as do the sequence of events surrounding it. Here, we made mutations in atlastin to selectively destabilize the crossover conformation and used fluorescence based kinetic assays to analyze the variants. All variants underwent dimerization and crossover concurrently, and at wild type rates. However, certain variants were unstable once in the crossover dimer conformation, and crossover dimer stability closely paralleled lipid-mixing activity. Tethering, however, appeared to be unimpaired in all mutant variants. The results suggest that tethering and lipid mixing are catalyzed concurrently by GTP hydrolysis, but that the energy requirement for lipid mixing exceeds that for tethering, and the full energy released through crossover formation is necessary for fusion.

Introduction

The substantial energy barriers that prevent spontaneous lipid bilayer fusion allow for the formation and maintenance of distinct subcellular compartments in eukaryotic cells. However, controlled fusion of these compartments must also regularly occur and so cells maintain a number of fusion catalysts that overcome these barriers. Fusion catalysts are typically integral membrane proteins that induce fusion by promoting the close apposition of opposing membrane bilayers and destabilizing the bilayers sufficiently to favor formation of the non-bilayer intermediates necessary for lipid mixing and membrane merger (Cohen and Melikyan, 2004; Frolov and Zimmerberg, 2010; Kozlov et al., 2010; Tamm et al., 2003).

Currently, the two best understood types of fusion catalysts are the viral fusion proteins, which mediate fusion between viral and host cell membranes during viral entry (Eckert and Kim, 2001; Skehel and Wiley, 2000; Weissenhorn et al., 2007), and the SNARE (soluble N-ethyl-maleimide-sensitive fusion protein attachment protein receptor) proteins, which mediate vesicle trafficking within the secretory and endocytic pathways (Chen and Scheller, 2001; Jahn and Scheller, 2006; Südhof and Rothman, 2009). Initially, viral fusion proteins reside solely in the viral membrane but then undergo a conformational rearrangement to insert into the host membrane, thus spanning the two membranes. In contrast, SNARE fusion begins with two separate entities each stably bound to the vesicle and target, with initial *trans* contacts forming a complex that spans both membranes. At first glance these two evolutionarily unrelated types of fusion catalysts appear to use differing strategies. However, following initial contact, close mechanistic parallels can be drawn (Sollner, 2004). Both undergo a series of highly favorable conformational rearrangements (Chen and Scheller, 2001; Eckert and Kim, 2001; Jahn and Scheller, 2006; Skehel and Wiley, 2000; Südhof and Rothman, 2009; Weissenhorn et al., 2007), whose energy is estimated

sufficient to overcome the 40-50k_BT energy barriers that hinder spontaneous membrane fusion (Carr et al., 1997; Cohen and Melikyan, 2004; Fasshauer et al., 2002; Gao et al., 2012; Kuzmin et al., 2001; Li et al., 2007; Liu et al., 2006; Markin and Albanesi, 2002; Yersin et al., 2003). By the end, each reaches a final stable conformation that can only exist in post fusion membranes (Stein et al., 2009; Sutton et al., 1998; Weissenhorn et al., 1998; Weissenhorn et al., 1999). In both of these cases the driving force for membrane fusion comes from the highly favorable protein-protein interactions that convert the catalyst from a 'pre-fusion' to 'post-fusion' state.

In the past several years a new type of fusion protein has come under increasing study, the dynamin-related integral membrane protein atlastin responsible for the homotypic fusion of ER membranes (McNew et al., 2013; Park and Blackstone, 2010). Structurally, atlastin is distinct from either of the previously studied fusion proteins. At the N-terminus it contains a globular GTPase head domain that directly couples GTP hydrolysis to fusion activity (Orso et al., 2009). The GTPase head, also likely the site of initial *trans* contacts between atlastin dimers on opposing ER membranes, is connected via a short linker to a fully folded three-helix bundle (3HB) (Bian et al., 2011; Byrnes and Sondermann, 2011), which is in turn anchored to the ER membrane by two closely spaced trans-membrane (TM) helices. Emerging from the membrane is a C-terminal tail containing an amphipathic helix with a propensity to insert into the lipid bilayer (Faust et al., 2015; Liu et al., 2012).

Atlastin also appears to undergo highly favorable structural rearrangements between what have been termed 'pre-' and 'post-fusion' conformations by analogy to previously studied fusion catalysts. In the so-called 'pre-fusion' state, observed in the form2 crystal structure of human atlastin1 (hATL1), two atlastin monomers interact in a head to head fashion with the 3HBs packed against their respective heads and

pointed away from the dimer interface (Bian et al., 2011; Byrnes and Sondermann, 2011). With an interfacial binding area of only 756Å^2, this extended dimer conformation could represent an initial encounter complex between atlastins in opposing membranes. A similar head to head configuration is present in the so-called 'post-fusion' state observed in the form3 hATL1 crystal structure, though the interfacial area between heads (1886Å^2) is more than twice that in the form2 'pre-fusion' dimer (Byrnes et al., 2013). A more dramatic difference in the 'post-fusion' state is that the 3HBs have been dislodged from their respective heads and are crossed over one another and with respect to the heads, having undergone a rigid body rotation about a central conserved proline residue in the linker. In the 'post-fusion' state, the close parallel alignment between 3HBs and the additional new contacts formed between the 3HBs and opposing heads creates a highly stable crossover dimer configuration with a substantial total interfacial binding area of 3852Å^2 (Bian et al., 2011; Byrnes et al., 2013; Byrnes and Sondermann, 2011). Though the TM domains are not present in the structures, it is hard to envision how the two molecules could adopt the 'post-fusion' conformation while remaining in separate membranes (Bian et al., 2011; Byrnes et al., 2013; Byrnes and Sondermann, 2011).

With their focus on the similarities with other fusion proteins, initial models for atlastin-catalyzed fusion had formation of the crossover conformer as the most likely source of energy for overcoming the barriers to fusion (Bian et al., 2011; Daumke and Praefcke, 2011). In those models, atlastin monomers were typically depicted to encounter one another in *trans* in the GTP-bound state. Thereafter, hydrolysis of the GTP would induce a series of conformational changes that would not only tighten the head to head binding interface, but also cause expulsion of the 3HBs from their respective heads. The 3HBs, now unconstrained, would be free to undergo a rigid body rotation culminating in formation of the crossover state (Byrnes et al., 2013), which would drive lipid mixing and fusion.

Additional studies, however, reveal further complexity to the fusion mechanism. A peptide that corresponds to the atlastin tail amphipathic helix inserts into membranes and destabilizes the bilayer, while mutations in atlastin that inhibit this insertion block lipid mixing, showing that the tail is critically involved in the fusion process (Faust et al., 2015; Liu et al., 2012; Moss et al., 2011). Furthermore, even conservative amino acid substitutions in the TM domain block lipid mixing, though the underlying cause is not known (Liu et al., 2012). Finally, kinetic analysis of GTP-catalyzed conformational changes within the soluble domain of hATL1 has suggested head to head dimerization and crossover to be catalyzed concurrently by GTP hydrolysis (Byrnes et al., 2013). Collectively, these observations have been interpreted through a different type of model in which atlastins on opposing membranes come together essentially already in a crossover-like state, with the crossover conformation serving as an initial tethering unit holding opposing membranes closely together, while subsequent membrane insertion of the tail amphipathic helix in conjunction with the TM domains carry out the work of membrane fusion (Byrnes et al., 2013). In this alternate model, the energy released on crossover formation might play a less critical role in fusion catalysis.

Here, we set out to test the importance of atlastin's crossover conformation for membrane fusion. We reasoned that if the binding energy of the crossover conformation were to play a critical role in fusion catalysis, then atlastin's fusion capacity should be exquisitely sensitive to progressive reductions in that binding energy. As a test, we generated a panel of localized point mutations within atlastin that might variably reduce, but not abolish, the stability of the crossover conformation. The effects of these mutations on crossover were assessed kinetically and their effects on atlastin's tethering and fusion activity determined. All mutant variants underwent crossover at rates indistinguishable from the wild

type. On the other hand, crossover dimer stability differed widely among mutant variants, with the reduction in dimer stability closely paralleling the reduction in fusion activity, demonstrating for the first time, the close coupling between the binding energy of the crossover conformation and fusion. Additionally, we observed concurrent head to head dimerization and crossover, confirming that tethering and fusion are triggered simultaneously by GTP hydrolysis (Byrnes et al., 2013). However, tethering was not noticeably impaired by destabilization of the crossover dimer, indicating a lower energy barrier for tethering than for fusion. Finally, the GTPase reaction rate was sensitive to the concentration of atlastin, consistent with the hydrolysis cycle depending, in some way, on dimerization. Together the results are consistent with a model of the atlastin fusion mechanism in which GTP hydrolysis within the *trans* dimer triggers the concerted formation of a tightly bound crossover dimer state. If the energy released through formation of this 'post-fusion' state is sufficient to mix the lipid bilayers, then fusion ensues; otherwise the reaction does not progress beyond tethering.

Results

Validation of a PIFE assay for crossover. Assays for atlastin crossover have largely been based on the close proximity and parallel alignment of the 3HBs occurring exclusively in the crossover conformation (Byrnes et al., 2013; Liu et al., 2015; Morin-Leisk et al., 2011; Saini et al., 2014). We previously engineered a cysteine residue (G343C) in the 3HB of the soluble domain (AA 1-415) of *Drosophila* atlastin (cytoDATL), and as anticipated based on the proximity of the 3HBs in the form3 hATL1 'post-fusion' crystal structure (Byrnes et al., 2013), a homo-bi-functional cross-linker with a short 8Å spacer arm conjugated two 3HBs only under conditions of crossover (Morin-Leisk et al., 2011; Saini et al., 2014). More recently, Förster Resonance Energy Transfer (FRET) between CFP and YFP fused C-terminally to the 3HB of the hATL1 soluble domain (cyto-hATL1- CFP/YFP) has been used to establish the kinetics of crossover under stopped flow conditions (Byrnes et al., 2013). Here as an alternate to the CFP/YFP sensors, we adapted a method termed Protein Induced Fluorescence Enhancement (PIFE). PIFE, used previously to monitor DNA-protein interactions, takes advantage of the environmental sensitivity of the Cy3 fluorophore (Gruber et al., 2000; Mujumdar et al., 1993). When DNA within 0-4nm of a protein-binding site is conjugated with Cy3, nearby protein binding reduces the torsional mobility of the Cy3, resulting in distance dependent fluorescence enhancement (Hwang et al.). When conjugated to G343C of cytoDATL, Cy3 underwent a ~20% fluorescence enhancement under conditions leading to crossover, as schematized (Fig 2-1A).

As PIFE had not been used previously to monitor crossover, it was important to validate that it works as expected based on previous data. A robust fluorescence enhancement was seen after mixing Cy3-cytoDATL with the non-hydrolysable GTP analog GMPPNP, but not GDP or buffer (Fig 2-1B). The time to

maximal enhancement ($t_{1/2}$ ~50 sec) was nearly identical to that previously observed for cyto-hATL1-CFP/YFP by FRET (Byrnes et al., 2013). When R48E, a mutation that abrogates nucleotide binding (Bian et al., 2011; Byrnes and Sondermann, 2011), was tested under the same conditions, no enhanced signal was observed with any nucleotide (Fig 2-1C), indicating that crossover, as reflected in the PIFE signal, was induced specifically by GMPPNP binding. Furthermore, as observed previously for cyto-hATL1-CFP/YFP (Byrnes et al., 2013), GTP gave a profound 100-fold acceleration of crossover over that seen with GMPPNP (Fig 2-1D). Thus, PIFE recapitulated key aspects of atlastin crossover, and corroborated an earlier report that GTP binding, and hydrolysis in particular, catalyzes atlastin crossover (Byrnes et al., 2013).

Previous work in our lab identified two charged residues important for crossover, K320 and E328 (Morin-Leisk et al., 2011; Saini et al., 2014). These residues, conserved between DATL and human atlastins, are at the heart of the crossover dimer and participate in an intra-molecular salt bridge in the 'post-fusion' conformation. We previously showed that the reversal of charge at either residue in cytoDATL (K320E or E328R) disrupts both crossover and fusion without diminishing steady state GTPase activity (Morin-Leisk et al., 2011; Saini et al., 2014). Interestingly, the compensatory double charge reversal mutation (K320E, E328R), predicted to restore charge attraction, appeared to fully restore crossover according to crosslinking assays (Morin-Leisk et al., 2011; Saini et al., 2014). Yet it only partially restored fusion activity (Saini et al., 2014). To test if PIFE might offer a more sensitive test for crossover and reveal a mild defect still present in the double mutant variant, we compared GMPPNP-induced PIFE in wild type, single (K320E), and double mutant (K320E, E328R) variants (Fig 2-1E). As anticipated, the single mutant variant was strongly impaired, while crossover was largely restored in the double mutant variant. However, a modest defect in crossover, not previously seen with crosslinking, was still observed in the double mutant variant, with the PIFE signal not yet reaching its maximal value

well after the wild type signal had plateaued (Fig 2-1E). Taken together, this data indicated that PIFE could be a powerful tool for detecting subtle defects in atlastin crossover.

Variable disruption of crossover. We next set out to create a panel of atlastin mutant variants with variable disruptions to the crossover state. In addition to being part of a salt bridge, K320 in the crossover dimer is at the heart of a highly spatially restricted bend in the linker between the GTPase head and the 3HB (Byrnes et al., 2013), making it an ideal focal point for additional mutagenesis (Fig 2-2A, B). Further, K320E shows no loss of steady state GTPase activity despite being defective in both crossover and fusion (Saini et al., 2014), making it an ideal residue to target the crossover conformation specifically. Finally, though we had shown that the creation of charge repulsion with the nearby E328 rendered the charge reversal of this residue (K320E) incapacitating for fusion (Saini et al., 2014), we found, surprisingly, that the salt bridge, per se, was nonessential for fusion (see Fig 2-7A below). Reasoning that a variety of uncharged amino acid substitutions of this residue may provide a range of defects possibly milder than K320E, K320 was replaced with T, M, G or N. We also included the previously partially characterized P317G variant (Saini et al., 2014) both because of the proximity of the conserved P317 residue to K320 and its unique position as the pivot point of 3HB rotation during crossover (Fig 2-2A, B). As anticipated based on previous GTPase assays of K320E and P317G (Saini et al., 2014), all variants had steady state GTPase activity similar to the wild type (Fig 2-S1).

The mutant variants were first analyzed using PIFE under conditions of accelerated crossover with GTP. In order to emphasize the relative rates of crossover across different mutant variants, the data were normalized to a value of 1 for maximum fluorescence and a value of 0 for minimum fluorescence. The kinetics of crossover was unaffected by normalization (see Fig 2-S2 for kinetics before (Fig 2-S2A) and

after (Fig 2-S2B) normalization). To our surprise, when GTP was added to initiate crossover, no significant difference in crossover rate was observed between the wild type and any mutant variant (Fig 2-2C). The main difference between variants was the magnitude of an early downward deflection that preceded the fluorescence enhancement due to crossover (Fig 2-2C'). For any given mutant variant, the slope of the downward deflection depended strongly on nucleotide concentration (Fig 2-2D), indicating nucleotide binding as its cause. Based on the proximity of the Cy3-labeled 3HB residue to the GTPase head in the form2 structure (Fig 2-2A), we suspected that this downward deflection could be due to a starting Cy3 fluorescence enhancement arising from packing interactions between the 3HB and head (Byrnes et al., 2013), which is subsequently lost as the position of the 3HB is altered upon nucleotide binding. Based on this reasoning, the differences in the magnitude of downward deflection across mutant variants could be attributed to slight differences in the extent to which the 3HB is initially packed against the head prior to nucleotide loading.

The lack of any differences in crossover rates for any of the variants (Fig 2-2C) implied that none were defective in crossover formation, per se. This was surprising, and we wondered whether defects might be better revealed with GMPPNP, which induces crossover 100-fold more slowly than GTP and showed clear differences between various salt bridge mutant variants (Fig 2-1E). When GMPPNP was used to initiate the reaction, crossover defects were readily apparent for K320N, K320G and P317G (Fig 2-3A,B). By contrast, K320M and K320T showed only a slight or modest defect, respectively. We concluded that some but not all of the targeted mutant variants had a defect in either forming or maintaining the crossover state. Given that the defect was evident only during the apparent slow approach to equilibrium induced by GMPPNP (Fig 2-3A,B), we suspected that the main defect in these variants might lie less in the formation, and more in the maintenance, of the crossover conformation.

Crosslinking confirms certain mutant variants accumulate more slowly in the crossover state. To confirm our observations with fluorescence, we returned to our original crosslinking assay in which we had shown the homo-bi-functional thiol reactive cross-linker BMOE to conjugate two 3HB G343C residues to one another exclusively in the crossover state (Saini et al., 2014). To increase the time resolution of the assay, the time of incubation with cross-linker was drastically shortened, from 30 minutes to 20 seconds. Additionally, we took advantage of the availability of cysteine reactive cross-linkers of longer lengths to probe for the possibility of more loosely crossed-over conformations, if present. After incubating each variant for either 60sec or 60min in the presence of GMPPNP, either BMOE, with an 8Å spacer arm, or MTS17, with a 24Å spacer arm (Loo and Clarke, 2001) was used to capture dimers (Fig 2-4A,B). Paralleling results with the PIFE assay with GMPPNP (Fig 2-3A,B), K320N, K320G and P317G variants were slower to accumulate crossover dimers as compared to wild type, K320M and K320T. Little or no early products were seen for the former, whereas for the latter, cross-linked products were observed as early as 60sec. Similar results were obtained with both short (Fig 2-4A) and long (Fig 2-4B) cross-linkers, indicating the absence of another discrete, loosely crossed over intermediate en route to full crossover. Finally, confirming previous crosslinking data (Saini et al., 2014) and the PIFE data above (Fig 2-1E), the charge reversal variant K320E showed only residual accumulation of crossover dimers with GMPPNP even after 60min. These data confirmed that the K320N, K320G and P317G variants had a defect in either forming and/or maintaining the crossover state.

The crossover conformation is destabilized in certain mutant variants. We next tested whether K320N, K320G and P317G might have a defect in crossover dimer maintenance that could account for the slowed approach to equilibrium seen with GMPPNP (Fig 2-3A). To assess crossover dimer stability, we

used FRET to monitor dimer dissociation rates. FRET between Alexa488 and Alexa647 on an engineered cysteine on the head of each monomer has been used previously to report on cyto-hATL1 head to head dimerization kinetics (Byrnes et al., 2013) and we adapted the assay here by targeting the equivalent cysteine residue (S270C) in cytoDATL. Alexa488 and Alexa647 labeled cytoDATL crossover dimers were first pre-formed with GMPPNP (Fig 2-5A). The use of the non-hydrolysable analog here was necessary to prevent rapid dimer disassembly, which is likely coupled to product release after GTP hydrolysis (Byrnes and Sondermann, 2011; Morin-Leisk et al., 2011; Moss et al., 2011). A 60min initial incubation period with GMPPNP was of sufficient length to ensure that all variants, even those slow to reach equilibrium, had attained their maximal extent of crossover as indicated by a plateau in both FRET and PIFE signals (Fig 2-8 below and Fig 2-3 respectively). This was followed by addition of excess unlabeled cytoDATL, which should produce a loss of FRET over time as labeled subunits that dissociate will re-form new dimers primarily with unlabeled subunits (Fig 2-5A). There was little or no loss of acceptor fluorescence when wild type crossover dimers were spiked with excess unlabeled wild type cytoDATL (Fig 2-5B) over that seen when spiked with buffer (Fig 2-5C), indicating that wild type crossover dimers formed with GMPPNP are stable over the course of 2h. This essential irreversibility contrasted with the relatively rapid turnover seen previously using the alternate non-hydrolysable analog GTP□S (Liu et al., 2015), which may possibly be explained by some hydrolysis of the GTP□S. In contrast to the wild type, K320N, K320G and P317G, the same variants slow to accumulate in the crossover state with GMPPNP (Fig 2-3 and Fig 2-4), showed accelerated disassembly over the course of 2h, indicating a loss of crossover dimer stability (Fig 2-5B). Dimerization was still favored for these variants, as indicated by the minimal loss of the FRET signal after buffer addition (Fig 2-5C). On the other hand, K320M and K320T were either indistinguishable from the wild type, or only slightly destabilized, respectively (Fig 2-5B). We concluded that the targeted mutant variants were variably diminished in crossover dimer stability, with WT ≈ K320M > K320T >> K320N > P317G > K320G. Moreover, the loss of crossover dimer stability for K320N,

K320G and P317G could account for the slowed accumulation of GMPPNP crossover dimers observed for these variants (Fig 2-3) as well as the lower extent of accumulation of crossover dimers for some of the variants even after 1h (Fig 2-4). Unlike the wild type crossover dimer, which formed essentially irreversibly, the mutant variant crossover dimers underwent significant dissociation, yielding a slowed approach to an equilibrium state of continued crossover formation and loss.

Crossover dimer stability closely parallels fusion activity. To assess the impact of reduced crossover dimer stability on atlastin function, we next looked at the fusion activity of these mutant variants. First we assessed ER network integrity in cells expressing each mutant variant as a proxy for *in vivo* fusion functionality (Saini et al., 2014). Typically, overexpression of any fusion incompetent atlastin results in a dominant negative disruption of the ER network and loss of network branching in some fraction of cells; whereas, overexpression of a fusion active atlastin causes little or no perturbation (Saini et al., 2014). Wild type and mutant versions of full length Venus-DATL were transfected into COS-7 cells and the fraction of overexpressing cells with a normal branched ER network morphology was visualized (Fig 2-6A) and quantified for each mutant variant (Fig 2-6B). K320M cells were indistinguishable from the wild type; a very small fraction of K320T cells showed ER defects; and ~50% of K320N cells showed substantial ER disruption. Meanwhile, virtually all K320G and P317G cells showed a loss of normal ER (Fig 2-S3 shows the full range of abnormal ER morphologies observed for these variants). Based on our prior work (Saini et al., 2014), the results predicted full fusion competence for K320M, slightly reduced fusion for K320T, only residual fusion for K320N, and absence of fusion activity altogether for K320G and P317G.

Fusion activity was directly assessed using a previously described *in vitro* lipid-mixing assay (Liu et al., 2015; Moss et al., 2011). The full-length version of each DATL variant was inserted at a 1:1000 protein:lipid ratio into either unlabeled lipid vesicles or vesicles with lipids containing the fluorophores Marina Blue (MB) and nitrobenzoxadiazole (NBD), with NBD acting to quench the MB. In the presence of GTP, mixing of labeled and unlabeled vesicles due to either full or hemi-fusion, leads to a de-quenching of the MB. The *in vitro* lipid mixing activity mirrored the *in vivo* results (Fig 2-7A). K320M had activity similar to the wild type, whereas K320T had a modest slowing. K320N was capable of some lipid mixing, but at severely reduced levels (Bian et al., 2011; Saini et al., 2014). Finally, K320G and P317G had undetectable activity. All variants were incorporated into vesicles with similar efficiency (Fig 2-S4). Overall, *in vitro* lipid mixing activity correlated remarkably well with crossover dimer stability. To convey the relationship between crossover dimer stability and fusion activity, the apparent dimer dissociation rate for each variant (Fig 2-5B), obtained by a fit to an exponential decay equation (Materials and methods), was plotted against its *in vitro* lipid mixing activity (Fig 2-7B). The plot underscored the striking correspondence between crossover dimer stability and fusion activity.

Tethering activity is less dependent on crossover dimer stability. The above results suggested that the binding energy of the crossover conformation is a key determinant of fusion capacity. However, it did not provide any information on potential impacts on membrane apposition, or tethering. To identify possible kinetic defects in tethering, we turned to a previously established assay based on an increase in light absorbance over time as vesicle tethering produces larger objects that scatter more light, thereby leading to an apparent increase in absorbance (Liu et al., 2015). A full-length version of each DATL mutant variant was inserted into lipid vesicles and the absorbance at 405nm monitored after GTP addition (Fig 2-7C). As expected (Saini et al., 2014), the nucleotide binding defective variant, R48E, showed no tethering activity whatsoever. Also as expected, the wild type, K320M and K320T variants all

showed robust tethering, with the magnitude of absorbance changes similar to previously reported values for the wild type (Liu et al., 2015). Though not shown here, the majority of the absorbance increase for these fusion active variants was expected to be due to vesicle tethering, with a minor fraction of the signal arising from increased vesicle size after fusion (Liu et al., 2015). Importantly, for the K320N, K320G and P317G variants, in which little or no signal was expected from fusion, the absorbance increased well above background levels and at a pace at least as robust as the wild type. The meaning of the differences in amplitude observed with different mutant variants was unclear, as the differences did not correlate with any other parameter; tethering activity and crossover dimer stability appeared to be inversely correlated for certain mutant variant pairs but not for others. Though these data did not rule out a contribution of the crossover binding energy towards tethering, they favored a model in which the energy required for fusion far exceeds that required for tethering; and crossover contributes a more important driving force for fusion.

Hydrolysis catalyzes simultaneous dimerization and crossover. Having established a major role for the crossover dimer conformation for fusion catalysis, we next set out to unravel the sequence of events surrounding crossover formation. Previous work on wild type hATL1 showed head to head dimerization occurring concurrently with crossover, suggesting that the two reactions are catalyzed simultaneously (Byrnes et al., 2013). Speculating that the destabilization of the crossover state in some of the variants might allow for the separation of dimerization and crossover as two rapid, but separable steps, we examined the GMPPNP-induced kinetics of head to head dimerization for each mutant variant using the FRET Alexa488 and Alexa647 donor/acceptor pair of cytoDATL described above. Consistent with the previous report (Byrnes et al., 2013), the kinetics of FRET were similar to the kinetics of PIFE for the wild type (Fig 2-8A), as well as for K320M and K320T (Fig 2-8B,C). However, for K320N, K320G and P317G (Fig 2-8D-F), the PIFE signal lagged substantially behind the FRET signal. This slowing of crossover

relative to head to head dimerization for K320N, K320G and P317G could have resulted from an uncoupling between head to head dimerization and crossover formation. Alternatively, it might have resulted from differences in the turnover of head to head and/or crossover dimer complexes during the slowed approach to equilibrium with GMPPNP that are not present with GTP.

To distinguish between these alternatives, we examined the kinetics when dimerization was initiated with GTP. Also, to minimize any potential issues in comparing PIFE with FRET kinetics, we replaced the PIFE probe with cytoDATL-mCerulean/SYFP FRET probes for crossover. When the reaction was initiated with GTP, the wild type kinetics of crossover as monitored by FRET was nearly identical to that seen above with PIFE (Fig 2-9A); though, as expected, the downward deflection in the PIFE signal caused by nucleotide binding (Fig 2-2C) was absent in the FRET signal. Consistent with the previous report (Byrnes et al., 2013), the rate of head to head dimerization as monitored by FRET was nearly the same as crossover FRET (Fig 2-9A); the slight difference was not statistically significant. Under these conditions, K320G, the most severely destabilized variant in the crossover state (Fig 2-5B), also showed concurrent head to head dimerization and crossover (Fig 2-9B). Furthermore, there was little or no difference between wild type and K320G in the initial rate of either head to head dimerization (Fig 2-9C) or crossover formation (Fig 2-9D). The fact that no difference could be discerned between wild type and K320G indicated that dimerization and crossover were inseparable even in the most severely defective variant, further corroborating a model in which dimerization and crossover occur simultaneously. In addition, the data underscored the highly selective nature of the K320G mutation in its ability to destabilize the crossover conformation without affecting any of the steps leading up to its formation.

Atlastin's GTPase cycle depends on dimerization. The apparent simultaneity of head to head dimerization and crossover formation seemed counterintuitive because it implied that unpaired atlastins from opposing membranes might enter into a *trans* crossover dimer configuration in a single step. However, an alternative interpretation was that atlastins first encounter one another in the GTP-bound state, whereupon hydrolysis is rapidly triggered to catalyze crossover dimer formation. If the initial interaction between GTP-bound heads were the rate-limiting step in the reaction cycle and subsequent steps ensue rapidly, then head to head dimerization and crossover formation would appear synchronous as observed (Fig 2-9A,B). Dimerization dependent hydrolysis of GTP has not been previously reported for atlastins. However, it has been established for human guanylate binding protein 1 (hGBP1), whose GTPase domain is more similar to atlastin than to any other dynamin-related protein (Zhao et al., 2001). Upon dimerization, the R48 residue in the P-loop of hGBP1, initially facing the dimer interface, swings into the nucleotide-binding pocket to stabilize the transition state (Ghosh et al., 2006). The same residue in atlastin (R77 in hATL1 and R48 in DATL) also faces out toward the dimer interface in the form2 'pre-fusion' structure but is oriented in toward the bound nucleotide in the form3 crossover dimer structure (Bian et al., 2011). Therefore it was tempting to speculate that dimerization dependent hydrolysis would have been conserved between these two closely related GTPases. To test for this possibility, we monitored the release of GDP at steady state as a measure of the GTPase activity of atlastin in a continuous coupled assay under saturating GTP concentrations but varying atlastin protein concentrations. Notably, as the concentration of cytoDATL fell below those typically used in GTPase assays of atlastin, the observed rate of product release fell accordingly (Fig 2-9E), with a fit of the rates to a simple dimerization equation yielding an estimated dissociation constant of ~0.45μM. While additional assays would be required to demonstrate the existence of a GTP-bound *trans* dimer, the apparent dependence of the hydrolysis cycle on dimerization was consistent with the possibility.

Discussion

Our results are summarized in a working model, essentially a hybrid of earlier models. The model starts with atlastins on opposing membranes (Fig 2-10A) encountering one another in a GTP-bound 'pre-fusion' conformation (Fig 2-10B), whereupon yet-to-be verified *trans* interactions between GTP-bound heads induce the rapid reorientation of catalytic residues necessary for GTP hydrolysis, which in turn triggers –in one step - the release of the 3HBs from the heads, strengthening of the head to head binding interface and 3HB crossover, to form the 'post-fusion' conformation (Fig 2-10C). In the case of the wild type or K320M atlastin, the free energy released through crossover formation, added to the membrane destabilizing effects of the TM domains and tail, is sufficient to simultaneously draw the membranes into close apposition and to initiate bilayer mixing for fusion (Fig 2-10C). By contrast, in the case of K320N, K320G or P317G, the binding energy of the crossover conformation is either largely insufficient, or insufficient altogether, to initiate bilayer mixing, leading to a state in which fusion has failed but the membranes remain tethered to one another (Fig 2-10C'). The first step of the model is largely based on the dimerization dependent hydrolysis of GTP observed for hGBP1 (Ghosh et al., 2006); and though consistent with our observations, requires further experimentation to confirm it. Other aspects of the model are supported by the following observations: 1) head to head dimerization and crossover formation occur concurrently; 2) mutant variants with a destabilized crossover conformation can generate a tethered state but are incapable of progressing to fusion; and 3) the binding energy of the crossover conformation closely parallels fusion capacity.

Even with its distinct architecture and enzymatic properties, a strong analogy can be drawn between atlastin and previously studied fusion protein catalysts, where a major driving force for membrane fusion

comes from a set of highly favorable protein-protein interactions that convert the catalyst from a 'pre-fusion' to 'post-fusion' state. The amount of energy released per atlastin crossover dimer, and how it compares to that of viral fusion protein and SNARE 'post-fusion' complexes, remains to be determined. For the SNAREs, the binding energy of the 'post-fusion' complex has been measured to be 30-40k_BT (Gao et al., 2012; Li et al., 2007; Liu et al., 2006; Yersin et al., 2003), remarkably similar to the theoretical 40-50k_BT estimated energy barriers for fusion (Cohen and Melikyan, 2004); though, due to the quasi-irreversibility of the 'post-fusion' states of both SNAREs and viral fusion proteins (Carr et al., 1997; Fasshauer et al., 2002), unconventional approaches have been required. The atlastin crossover dimer seems at least qualitatively similar, with no apparent dissociation over the course of 2h. It will be of interest in future studies to apply to atlastin the kinds of approaches used for the other fusion proteins.

It should be noted that our working model stems from the results of assays both in the soluble phase and those in the context of membranes. Tethering and fusion reactions are carried out, by definition, using the full-length protein anchored in vesicle membranes. However, preparing the full-length protein in vesicles appropriately labeled for the same kinds of assays that have been carried out in the soluble phase remains a challenge. Therefore the kinetic behavior of atlastin in the context of membranes is extrapolated from that in the soluble phase and the full effects of the added load of the lipid bilayer will need to be assessed in future work. For instance, the extent to which membrane-anchored atlastin achieves the tight crossover conformation seen in the form3 crystal structure as it undergoes fusion catalysis remains to be seen. Moreover, crossover formation in the soluble phase remained favorable even in the face of mutations that were destabilizing to the crossover state; however, the effects of membrane load on the favorability of crossover formation remain unknown. Presumably, crossover formation will be much less favored when coupled to the work of membrane fusion catalysis.

Finally, while this study has focused on the role of crossover in fusion, it cannot be overstated that fusion catalysis requires more. As noted above, membrane insertion of an amphipathic helix in the C-terminal tail of atlastin is also required (Faust et al., 2015; Liu et al., 2012) as are specific residues in the TM domain. As neither crossover formation, nor the tail, nor the precise sequence of the TM domain is required to reach the tethered state (Liu et al., 2015; Saini et al., 2014), but all are required for fusion (Faust et al., 2015; Liu et al., 2012; Saini et al., 2014), it may be that all of these mechanisms work in close conjunction and collectively to reduce the energy barrier to lipid mixing. In the absence of any one of these energetic contributions, the activation energy for fusion may be too high, thereby preventing fusion catalysis. Indeed crossover dimer formation, likely closely coupled to the initiation of bilayer mixing, may fail to occur altogether in the absence of the energetic contributions of either the tail or TM domain. *Trans* interactions between opposing membrane-spanning domains could provide an additional driving force, though it is currently not known whether the *trans* interactions of the atlastin crossover dimer extend into the TM region as proposed for previously studied 'post-fusion' complexes (Stein et al., 2009; Tamm, 2003). Furthermore, as the atlastin fusion mechanism is ultimately driven by GTP hydrolysis, the maximum free energy liberated by a single atlastin dimer during crossover is unlikely to exceed the total energy of hydrolysis of 2 molecules of GTP, thus unlikely sufficient on its own to offset the estimated activation energy (40-50k_BT) for fusion. *Cis* interactions between the membrane spanning domains, previously reported to occur independently of GTP (Liu et al., 2012), may help coordinate the activity of multiple atlastin dimers. A full understanding of the atlastin fusion mechanism will require the identification of all these additional binding interactions and their relative energetic contributions.

Figures

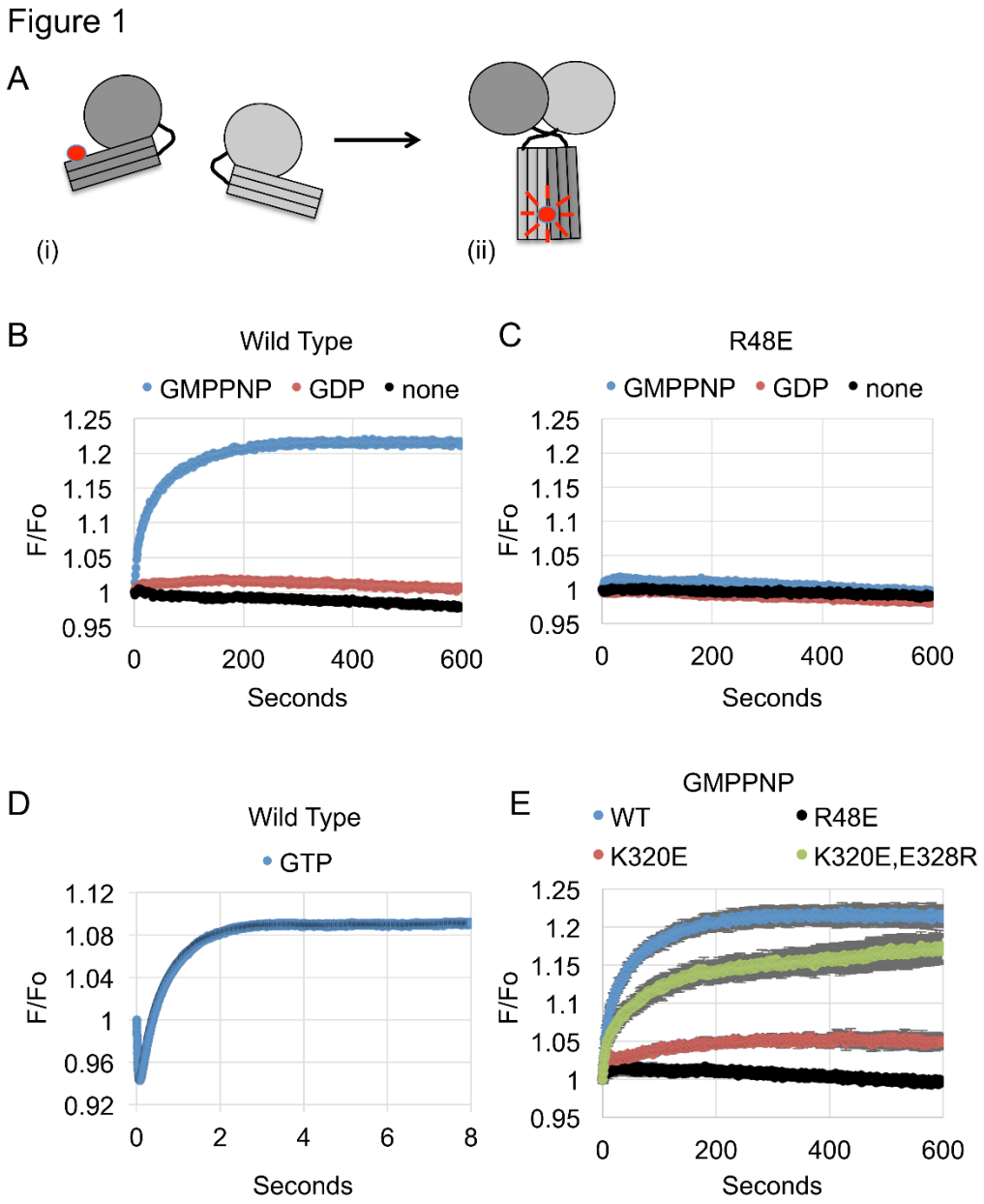

Figure 2-1. PIFE assay for crossover. (A) A schematic of Cy3 fluorescence enhancement as a cytoDATL monomer labeled with Cy3 on an engineered G343C residue in the 3HB (i) undergoes dimerization and crossover (ii). (B,C) PIFE, or fluorescence enhancement (F/Fo), over time for either wild type (B) or R48E (C) Cy3-cytoDATL mixed with the indicated nucleotides. (D) F/Fo over time when wild type Cy3-cytoDATL is mixed with GTP. (E) F/Fo over time when wild type, R48E, K320E, or the double mutant variant K320E,E328R is mixed with GMPPNP. For all assays, final concentrations following mixing were 2µM Cy3-cytoDATL and 1mM nucleotide. Either a single representative trace (B-D) or the average of 3 replicates (±s.e.m.) is shown (E).

Figure 2

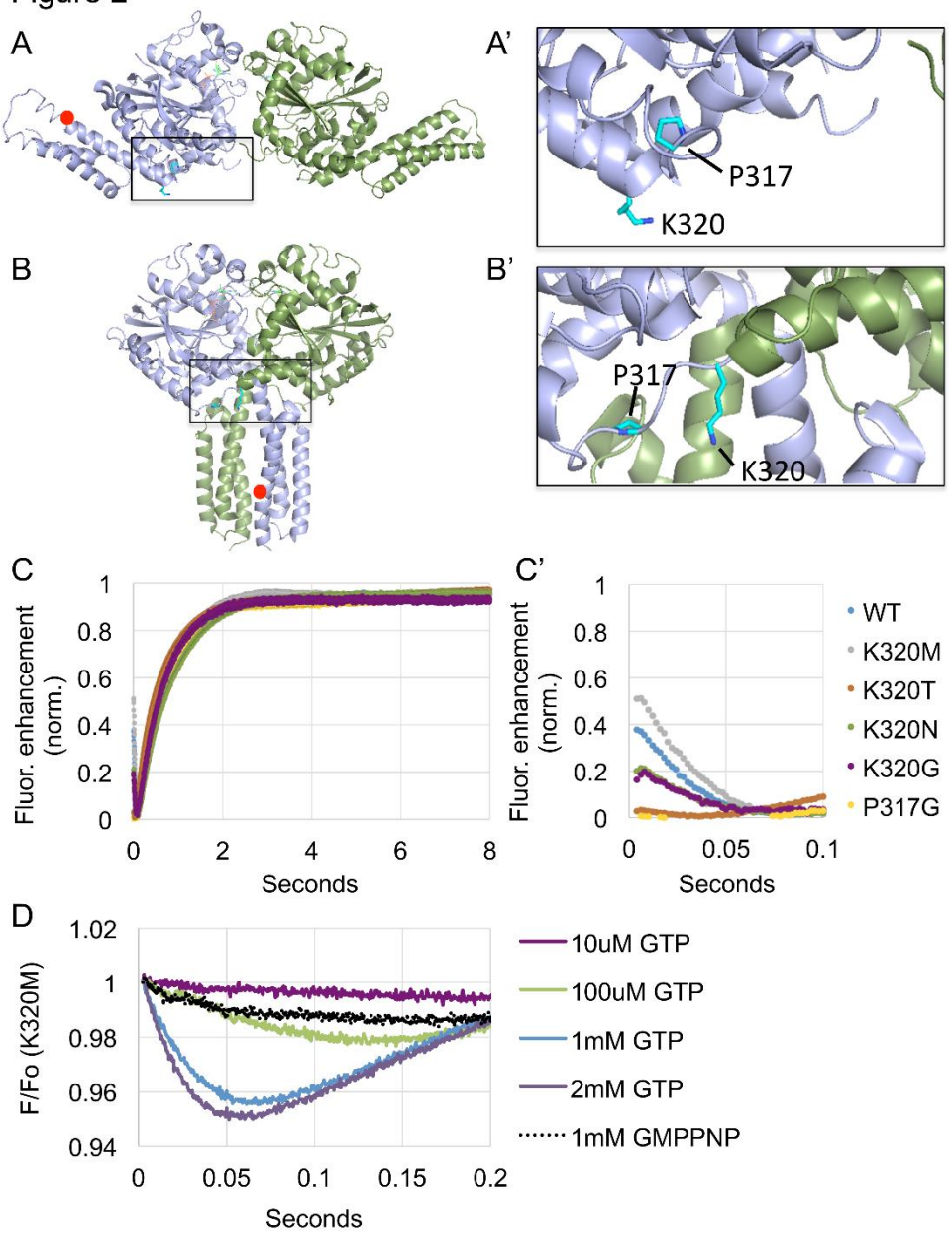

Figure 2-2. Mutant variants show no defects in GTP-catalyzed crossover formation. (A,B) The positions of K320 and P317 mutations made to target DATL crossover superimposed onto PyMOL renderings of (A) the hATL1 form2 extended dimer PDB 3QOF and (B) the hATL1 form3 crossover dimer PDB 4IDP. The position of the Cy3 dye in each structure is indicated with a red circle. (A',B') Enlargement of the boxed regions in (A,B) showing the K320 and P317 side chains highlighted in cyan. (C) Normalized PIFE over time when each of the indicated Cy3-cytoDATL mutant variants is mixed with GTP. (C') Zoomed in view of the first 100msec of the trace in (C). The average of 7 runs is shown for each trace (s.e.m.<0.01) and all traces were repeated with independent protein preps with similar results. (D) A single representative PIFE trace over time when K320M Cy3-cytoDATL is mixed with the indicated concentrations of GTP or GMPPNP. The final concentrations following mixing were 2µM Cy3-cytoDATL and 1mM nucleotide unless indicated otherwise.

Figure 3

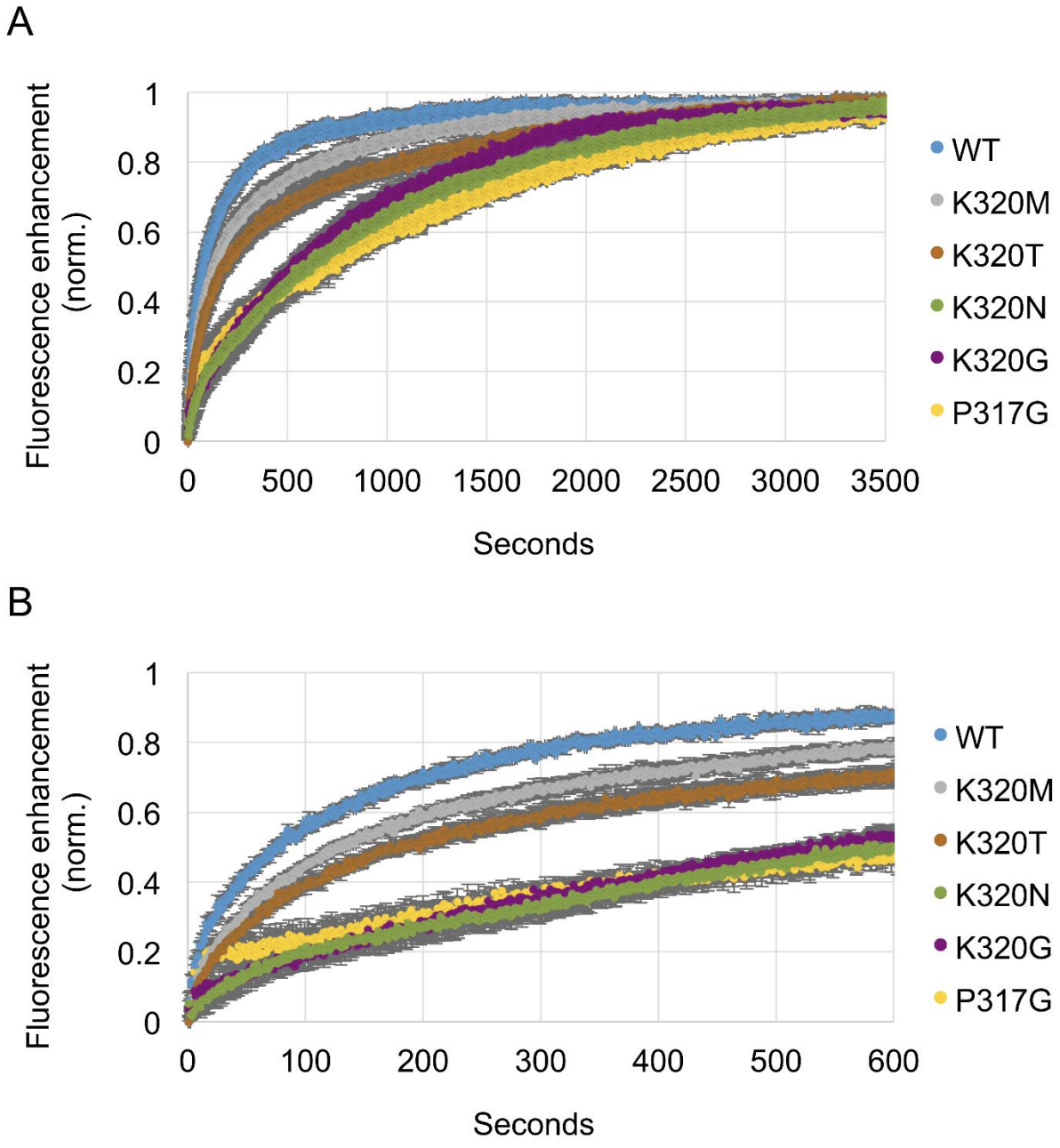

Figure 2-3. Mutant variants show defects in GMPPNP-induced crossover. (A) Normalized PIFE (n=3 replicates, ±s.e.m.) over time when each of the indicated Cy3-cytoDATL variants is mixed with GMPPNP. (B) Zoomed in view of the first 600sec of the trace in (A). Final concentrations following mixing were 1µM Cy3-cytoDATL and 1mM nucleotide. All traces were repeated with independent protein preps with similar results.

Figure 4

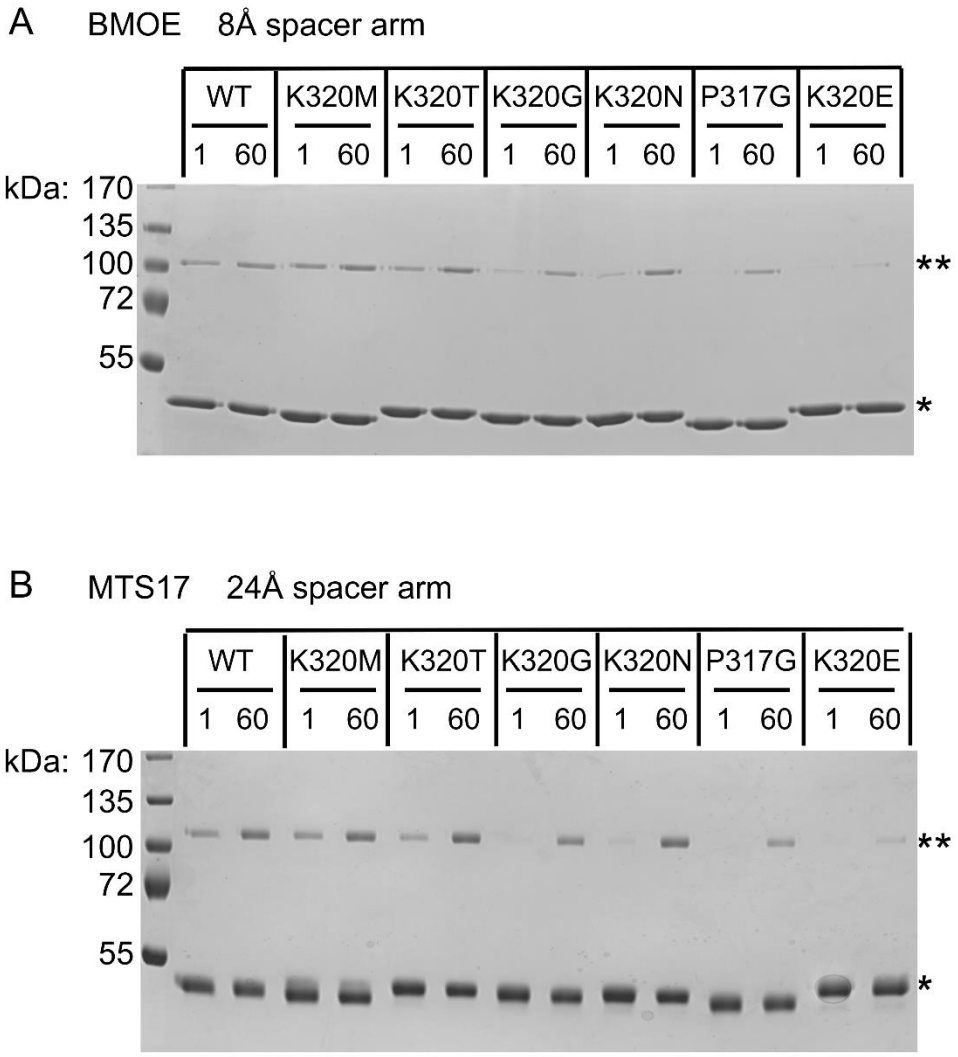

Figure 2-4. Crosslinking confirms crossover defects for a subset of mutant variants. Each of the indicated cytoDATL variants was incubated at RT for either 1min or 60min in the presence of GMPPNP and then subjected to 20sec of crosslinking with either BMOE (8Å spacer arm) or MTS17 (24Å spacer arm). The structure of each cross-linker is shown to the right. Cross-linked dimers were resolved by SDS-PAGE and visualized with Coomassie Blue. The single asterisk marks the monomer and the double asterisk marks the cross-linked dimer. All variants had the G343C substitution. Concentrations prior to cross-linker addition were 2µM CytoDATL and 1mM nucleotide. The data shown are representative of at least two independent experiments.

Figure 5

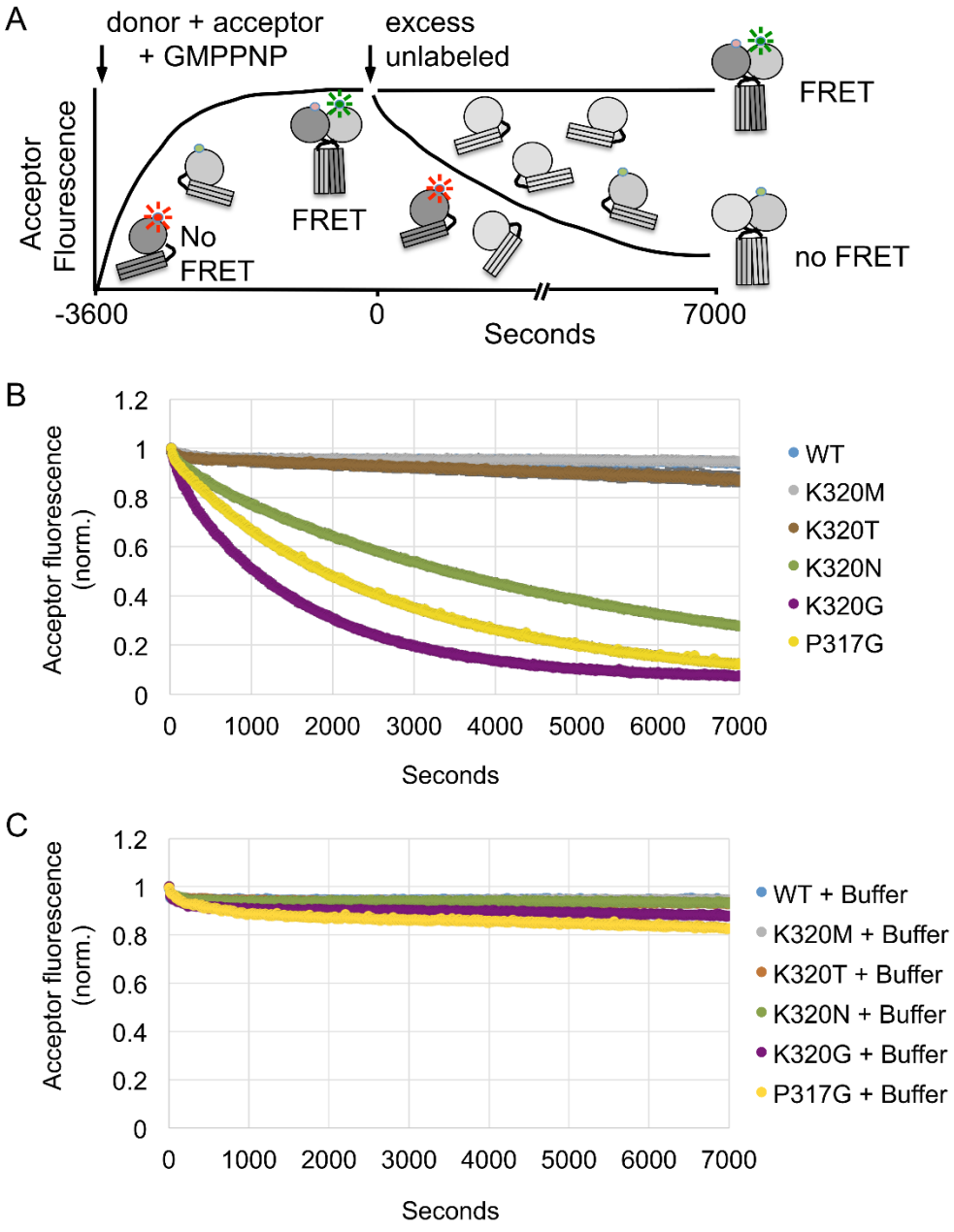

Figure 2-5. A subset of mutant variants has decreased crossover dimer stability. (A) Schematic of the assay. The indicated cytoDATL variants (2μM) labeled with Alexa488/647 at a 1:1 donor:acceptor ratio were incubated with 1mM GMPPNP (final concentrations) for 60min to form crossover dimers. After confirming that the FRET-induced acceptor fluorescence signal had plateaued, a five-fold molar excess of the corresponding unlabeled cytoDATL mutant variant was added and the subsequent decay in acceptor signal monitored over time. (B,C) Loss of acceptor fluorescence (n=3 replicates, ±s.e.m.) after addition of either the corresponding unlabeled competitor protein (B) or buffer (C).

Figure 6

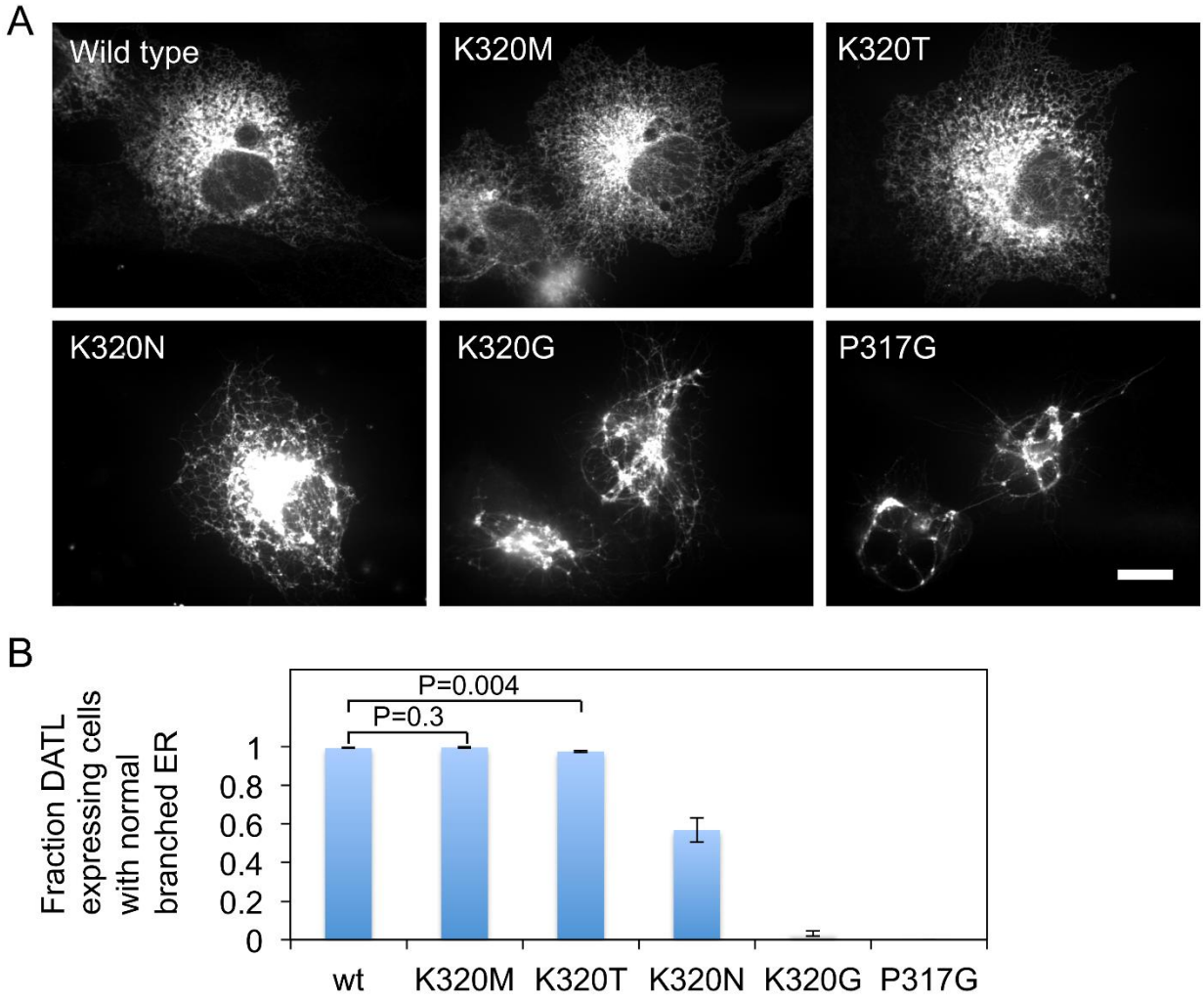

Figure 2-6. A subset of mutant variants causes abnormal ER network structure. (A) COS-7 cells transfected with each indicated variant of full-length Venus-tagged DATL were fixed and imaged 48 h later by confocal microscopy. Scale bar: 10µm. (B) Quantification of the percent of expressing cells displaying a normal branched ER, >100 cells per measurement, average of three independent measurements ±SD. *, P<0.0001 (Student's t-test) with respect to wild type.

Figure 7

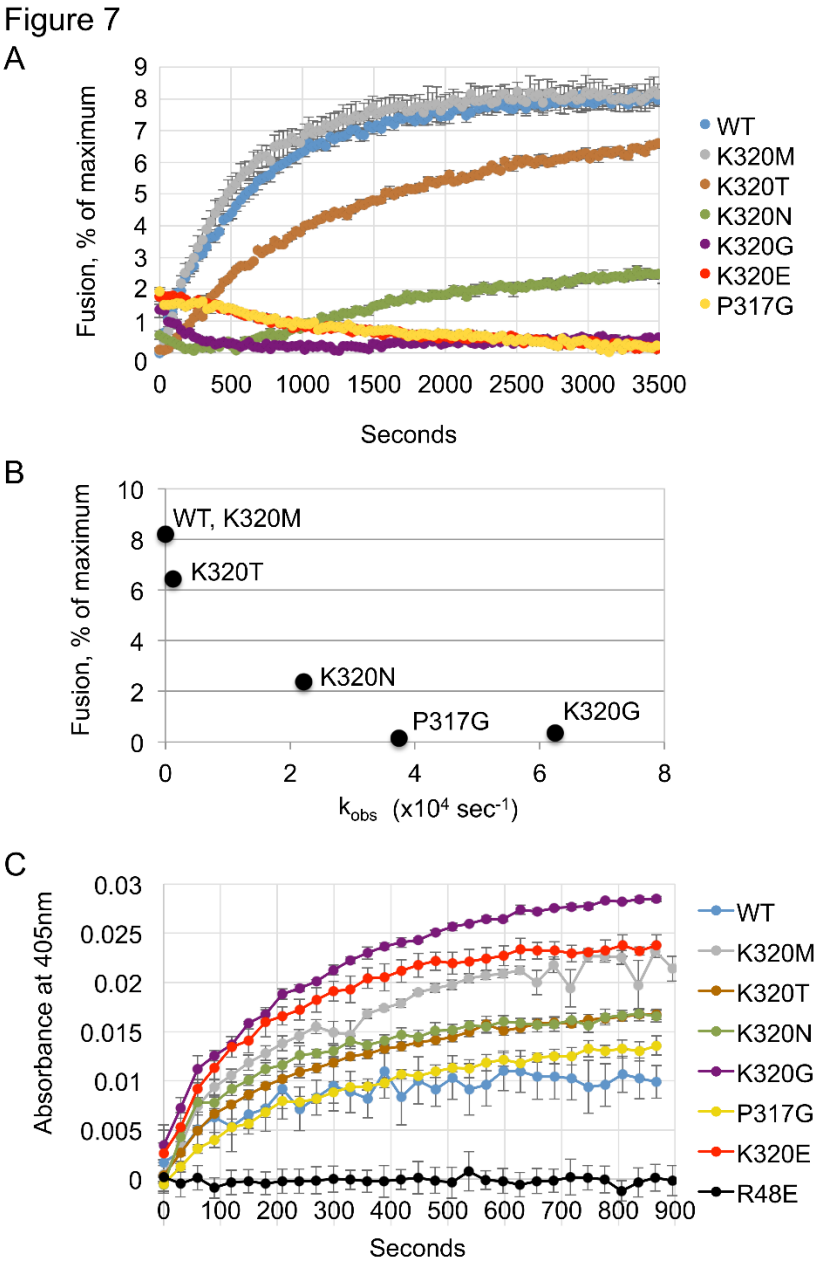

Figure 2-7. Crossover dimer stability correlates more closely with fusion than tethering. (A) Mutant variants are variably defective in *in vitro* fusion activity. The full-length DATL version of each mutant variant was reconstituted into donor and acceptor vesicles at a 1:1000 protein:lipid ratio. Fusion was monitored as the de-quenching of marina blue-labeled lipid present in the donor vesicles (0.6mM total lipid) over time after addition of 1mM GTP (n=3 replicates, ± s.e.m.). (B) Fusion activity closely parallels crossover dimer stability. The apparent dissociation rate constant for each variant, calculated by fitting the average of 3 traces (from Fig 2-5B) to an exponential decay equation (Materials and methods), is plotted against the average percent fusion (s.e.m.<0.3%) *in vitro* (endpoint of Fig 2-7A) achieved by the same variant. (C) Vesicle tethering activity does not correlate with crossover dimer stability. The full-length DATL version of each mutant variant was reconstituted into vesicles at a 1:1000 protein:lipid ratio (0.6mM total lipid). Tethering by each variant was monitored as the increase in 405nm absorbance over time after addition of 1mM GTP (n=3 replicates, ± s.e.m.).

Figure 8

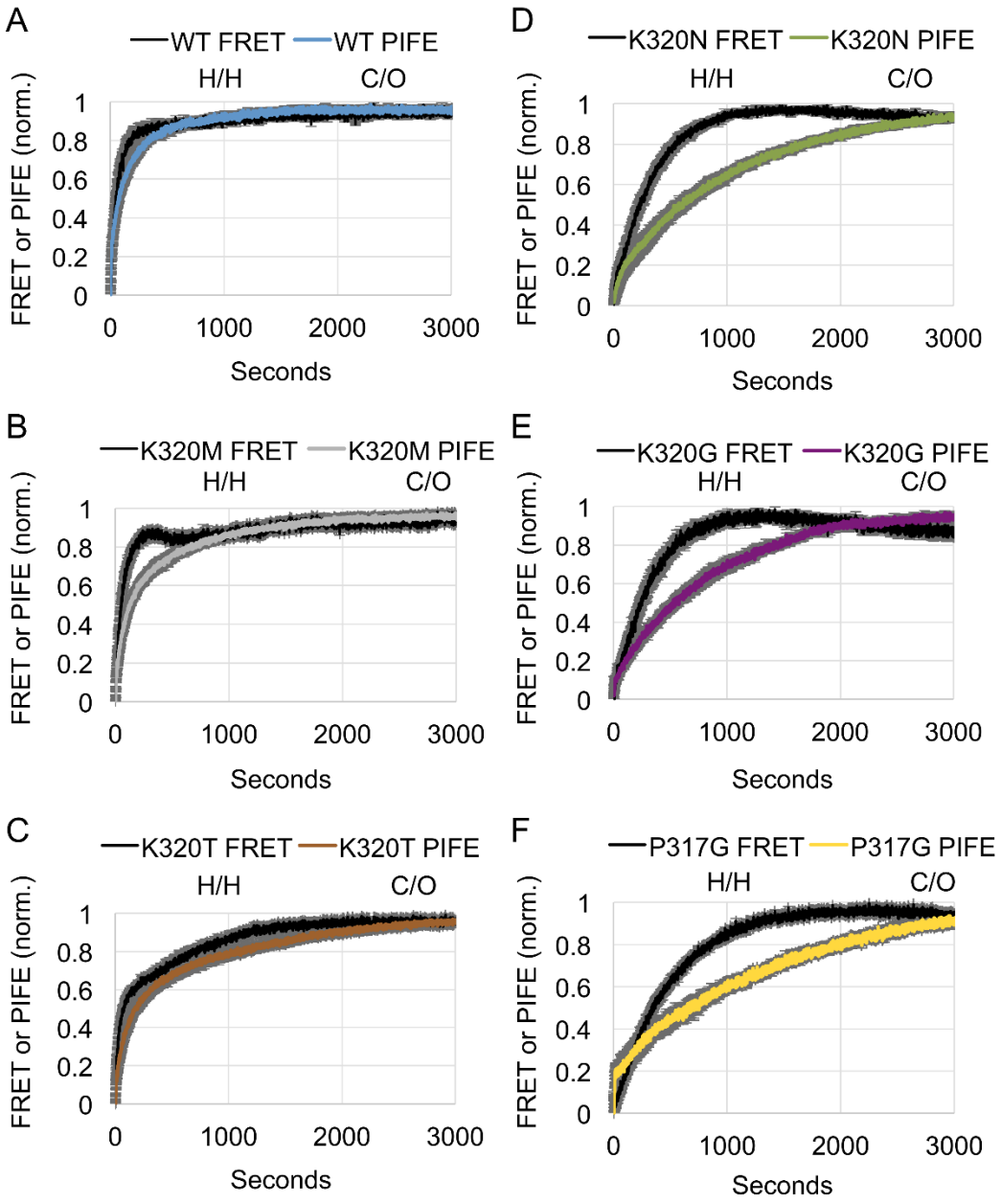

Figure 2-8. Head to head dimerization occurs prior to crossover when initiated with GMPPNP. Measurements of head to head dimerization monitored by FRET between (A) wild type, (B) K320M, (C) K320T, (D) K320N, (E) K320G and (F) P317G cytoDATL variants. Normalized FRET efficiency, E = 1 - (I_{DA}/I_D), over time, from mixing 1μM of the indicated variants with 1mM GMPPNP, are shown relative to the normalized PIFE traces for each variant obtained above using the same concentrations of protein and nucleotide (Fig 2-3A). The average of 3 replicates (±s.e.m.) is shown and the entire set of traces was repeated with independent protein preps with similar results.

Figure 9

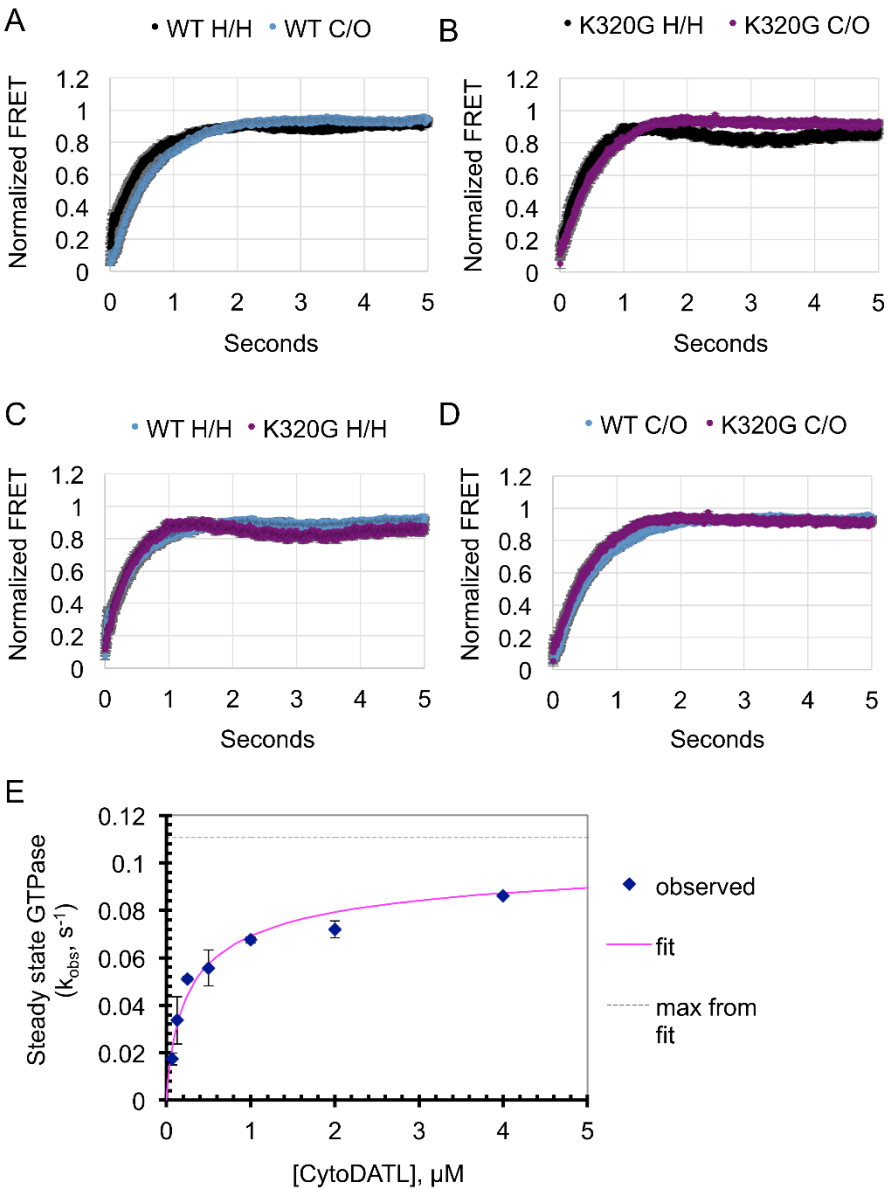

Figure 2-9. GTP hydrolysis is concentration dependent and stimulates simultaneous dimerization and crossover. Relative kinetics of head to head dimerization and crossover in wild type (A) and K320G cytoDATL (B) as monitored using FRET. Normalized FRET efficiency, $E = 1 - (I_{DA}/I_D)$, over time after mixing 1µM of the appropriate FRET pairs, cytoDATL-Alexa488/647 for head to head dimerization and cytoDATL-mCer/SYFP for crossover, of the indicated variants with 1mM GTP. Also shown are comparisons between the wild type and K320G with respect to head to head dimerization (C) and crossover (D), respectively. The average of 7 replicates (±s.e.m.) is shown and the entire set of traces was repeated with independent protein preps with similar results. (E) CytoDATL steady state GTPase activity varies with protein concentration. The observed GTPase activity (µM GDP sec^{-1} per µM cytoDATL) at the indicated concentrations of cytoDATL (n=3 replicates, ±S.D.) are plotted and fit to a simple dimerization equation. The data shown are representative of 2 independent experiments.

Figure 10

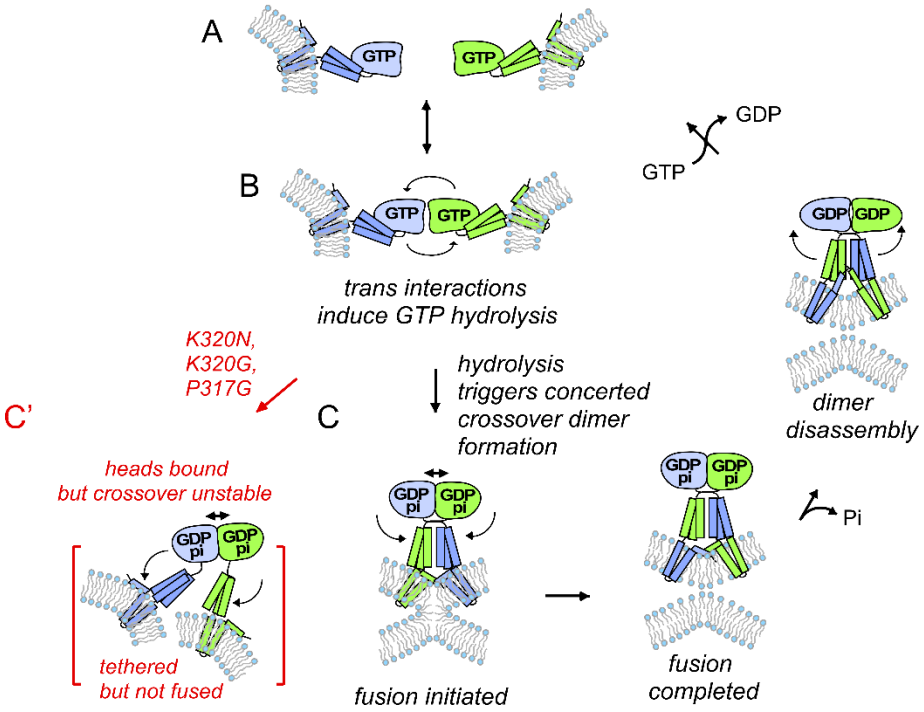

Figure 2-10. Working model for atlastin-catalyzed membrane fusion. GTP-bound atlastins on opposing membranes (A) encounter one another (B). This induces GTP hydrolysis, which triggers simultaneous tightening of the head to head interface and formation of the crossover dimer to initiate membrane fusion (C). When the crossover conformation is destabilized by the indicated mutations, fusion fails, resulting in a tethered state (C').

Supplemental Figure 1

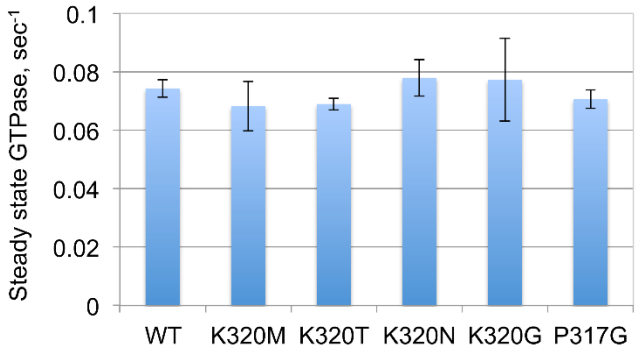

Figure 2-S1. All mutant variants have similar steady state GTPase activity. The indicated cytoDATL mutant variants (1µM) were incubated with 1mM GTP and subjected to a coupled enzyme assay (Materials and methods) measuring the production of GDP over time (µM GDP sec^{-1} per µM cytoDATL).

Supplemental Figure 2

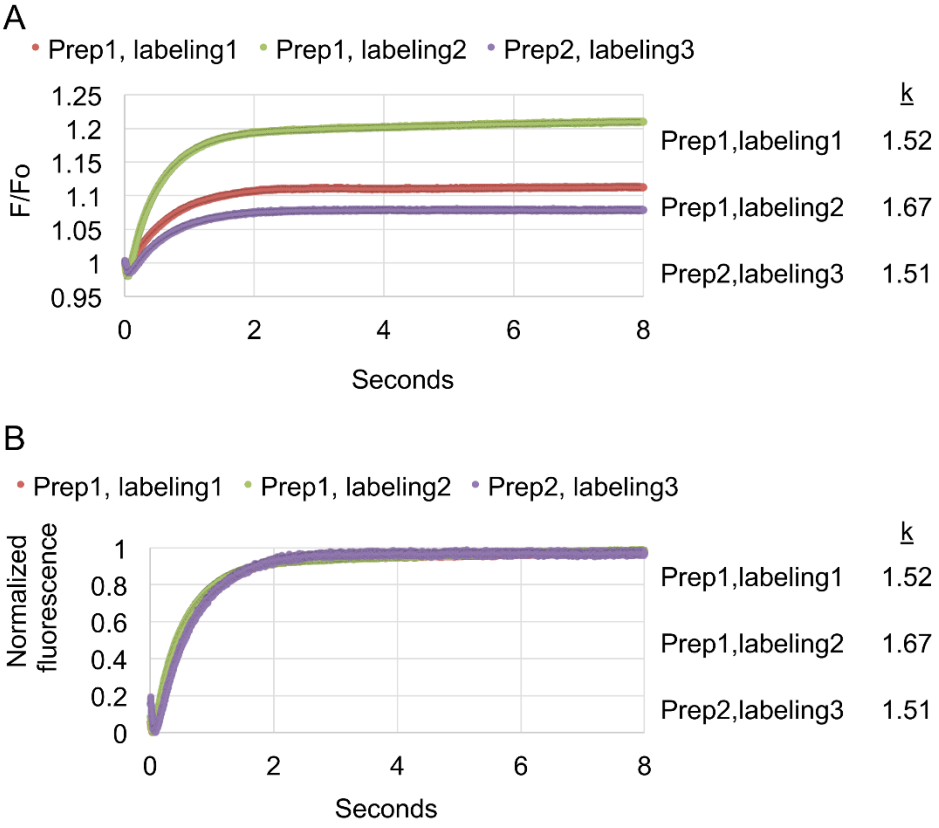

Figure 2-S2. Normalization has no effect on reaction kinetics of PIFE. (A) PIFE, or fluorescence enhancement (F/Fo), over time when 1μM K320G Cy3-cytoDATL from 3 independent labeling reactions and 2 independent protein preps is mixed with 1mM GTP. (B) The same data in (A) after normalization. A comparison of the reaction rates, k, from fitting the rising component of each trace to a single exponential decay equation, for each trace either before (A) or after (B) normalization, indicates that normalization has no effect on the reaction kinetics.

Supplemental Figure 3

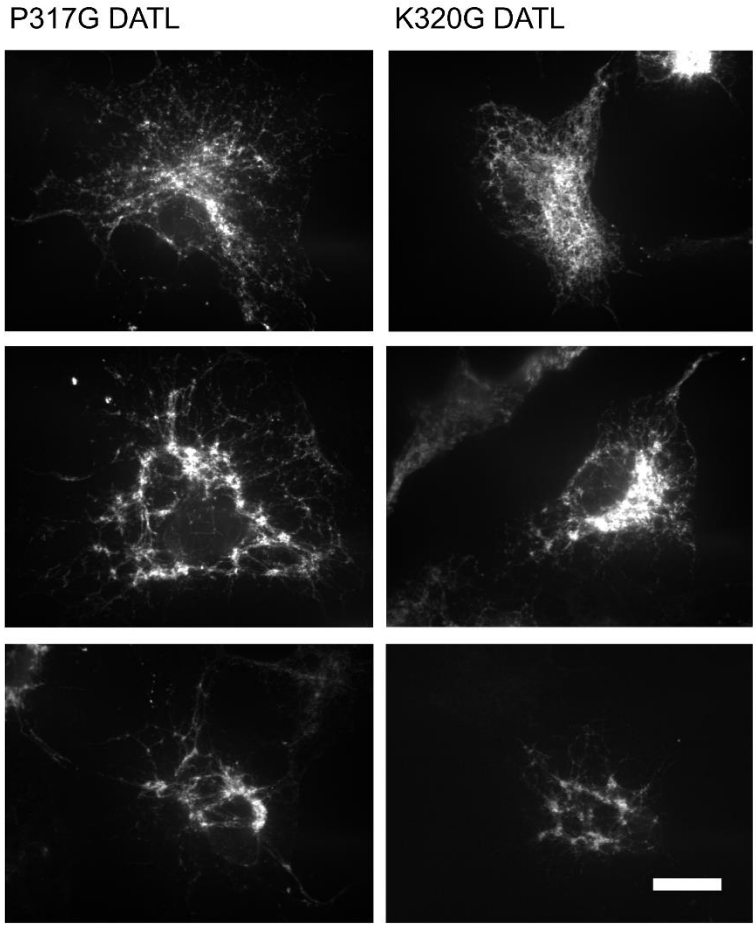

Figure 2-S3. Expression of P317G and K320G DATL causes a range of defective ER morphologies. COS-7 cells transfected with either P317G or K320G full-length Venus-tagged DATL were fixed and imaged 48 h later by confocal microscopy. Scale bar: 10µm.

Supplemental Figure 4

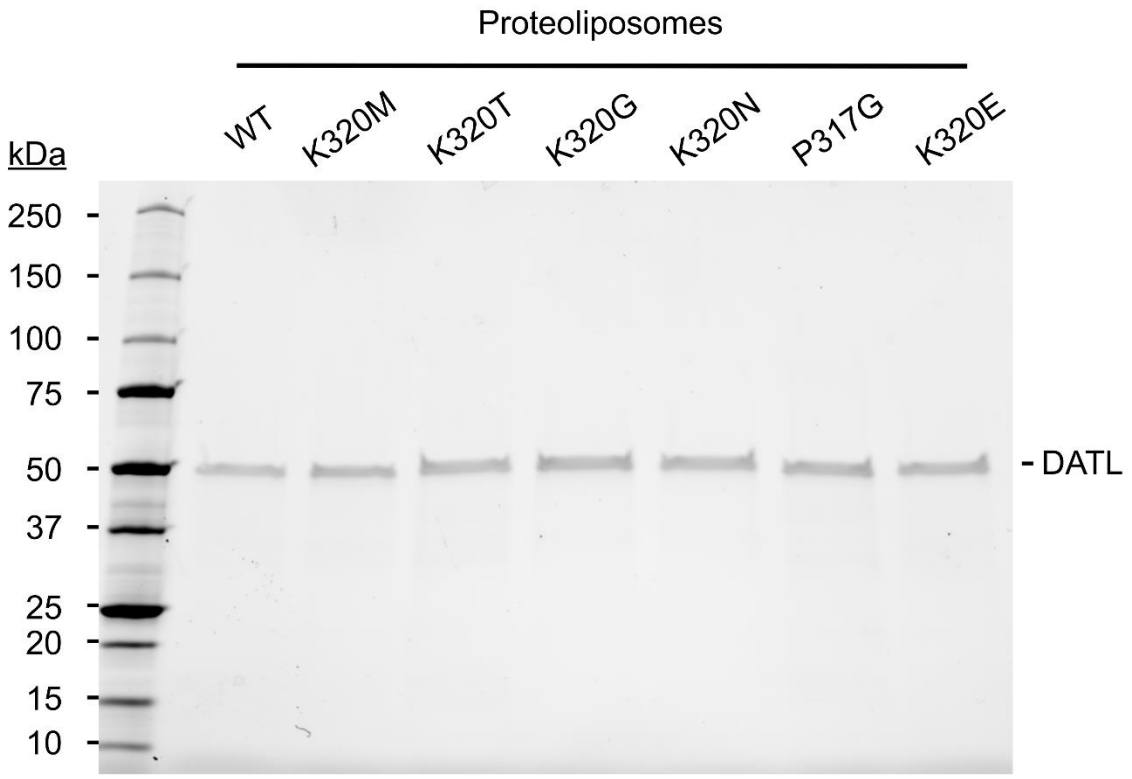

Figure 2-S4. All mutant variants of full length DATL are efficiently incorporated into vesicles. The indicated DATL proteins, purified and incorporated into labeled (donor) and unlabeled (acceptor) vesicles at a 1:1000 protein:lipid ratio were subjected to a (50%/45%/0%) Nycodenz flotation step gradient to separate incorporated from unincorporated protein. After desalting, equivalent amounts of each sample were resolved by SDS-PAGE and visualized with UV-induced tryptophan-bound trihalo fluorescence. Only the unlabeled vesicles are shown.

Materials and methods

Cells, constructs and reagents. Cell expression studies were in COS-7 cells maintained at 37°C in a 5% CO_2 incubator in DMEM (Sigma-Aldrich, St. Louis, MO) with 10% fetal bovine serum (Atlanta Biologicals, Atlanta, GA) and 1% penicillin/streptomycin (Thermo Fisher Scientific, Waltham, MA). The following constructs were considered wild type for their respective assays, with further mutations created using QuikChange mutagenesis (Qiagen, Valencia, CA) and confirmed through sequencing of the full construct (GENEWIZ, South Plainfield, NJ). All PIFE, crosslinking and GTPase assays used a previously described (Saini et al., 2014) 6xHis-tagged *Drosophila melanogaster* atlastin (DATL) soluble domain construct (AA 1-415) cloned into the pRSETB vector at NheI and EcoRI sites and containing an engineered cysteine at G343C in the 3HB. FRET assays for head to head dimerization used the same construct as for PIFE except that it lacked the G343C mutation and instead had an engineered cysteine S270C based on an equivalent mutation previously described in human atlastin1 (Byrnes et al., 2013). FRET assays for crossover used the same construct as for PIFE but lacking the G343C mutation and with either mCerulean3 (mCer3) or Super Yellow Fluorescent Protein (SYFP) at the C-terminus. These were generated by QuikChange insertion of a linker sequence encoding the AA's GTSTSGHG after AA415 of DATL followed by an NcoI site, into which the pcr-amplified coding sequence of mCer3 or SYFP (AA2-end) was inserted. Cell expression studies used a previously described N-terminally tagged Venus-DATL construct (Faust et al., 2015; Saini et al., 2014). Fusion and tethering assays used a previously described 6xHis-tagged full length DATL construct in a background of the following mutations: G343C, C429L, C452L, C501A, C350A, where the parent construct was generated by cloning a pcr-amplified fragment coding for DATL AA1-541 into the NheI and EcoRI sites in pRSETB. This cysteine substituted construct has fusion activity similar to the parent wild type (Saini et al., 2014). All lipids were purchased from Avanti Polar Lipids (Alabaster, AL). Nucleotides were purchased from Sigma-Aldrich, reconstituted to

100mM stocks in 10mM Tris, 1mM EDTA (pH8.0), and stored at -80°C. GTP for the GTPase assay was an exception, reconstituted to 40mM in 50mM Tris, 40mM $MgCl_2$ (pH8.0), adjusted to pH7. BMOE (bismaleimidoethane) was purchased from ThermoFisher Scientific and MTS17 (3,6,9,12,15-pentaoxaheptadecane-1,17-diyl bismethanethiosulfonate) was from Toronto Research Chemicals (Downsview, ON, Canada).

Protein expression and purification. Expression and purification of DATL was performed as previously described (Morin-Leisk et al., 2011; Saini et al., 2014). In short, DATL expression used a pRSETB vector in BL21(DE3)pLysS *E. coli*. Cells were grown at 25°C to OD~0.5 and induced with 0.5mM (for cytoDATL) or 0.2mM (for full length DATL) isopropyl β-D-1- thiogalactopyranoside (IPTG). Following induction cells were allowed to express atlastin either overnight at 20°C (cytoDATL) or for 2.5h at 16°C (full length DATL). Purification of the soluble domain used standard protocols and buffers for the purification of 6xHis tagged proteins on Ni-NTA Agarose (Qiagen). Purification of the full-length protein used the following modifications of the standard protocol: Cells were lysed in 4% Triton X-100 (Roche, Basel, Switzerland) in the standard lysis buffer, all wash buffers contained 0.1% Triton X-100, and elution was in 50mM Tris (pH 8.0), 250mM imidazole, 100mM NaCl, 5mM $MgCl_2$, 10% glycerol, 2mM 2-mercaptoethanol, 0.1% Anapoe-X 100 (Affymetrix, Santa Clara, CA) and 1mM EDTA. Peak fractions typically 4-8mg/ml (~1mg per liter culture) were flash frozen in liquid N_2 and stored at -80°C.

Fluorescence microscopy. COS-7 cells grown on 12mm glass coverslips (24-well plate, 0.5ml volume per well) were transfected with 100ng of the indicated Venus-DATL plasmids and 1.5µl of Lipofectamine 2000 transfection reagent (Life Technologies, Thermo-Fisher Scientific) according to the manufacturer's instructions. Cells were fixed with 3% paraformaldehyde 48h later and images were acquired with a spinning-disk confocal scanhead (Yokagawa; PerkinElmer, Akron, OH) mounted on an Axiovert 200

microscope (Zeiss, Thornwood, NY) with a 100x 1.4 NA objective (Zeiss) and acquired using a 12-bit ORCA ER camera (Hamamatsu Photonics, Hamamatsu City, Japan). Maximal value projections of sections at 0.2µm spacing were acquired using Micro-manager open-source software (University of California, San Francisco, San Francisco, CA).

Fluorescent dye Labeling. For PIFE, cytoDATL containing an engineered cysteine at G343C was desalted by centrifuging through a 5mL column (Pierce, Thermo Fisher Scientific) containing 4mL bed volume of Sephadex G-25 (Sigma-Aldrich) pre equilibrated with labeling buffer (25mM tris pH 7.0, 100mM NaCl, 5mM $MgCl_2$, 2mM EGTA, 1mM imidazole, 500µM TCEP). Cy3 maleimide (GE Healthcare, Thermo Fisher Scientific) was added at a 1:1 protein:dye molar ratio. The reaction was incubated for 2h at room temperature before being spun at 100,000rpm (TLA100 rotor, Beckman Coulter, Indianapolis, IN) for 15 minutes at 4°C to remove any precipitate. Labeled cytoDATL was then desalted twice through a column pre equilibrated with SEC buffer (25mM tris pH 7.0, 100mM NaCl, 5mM $MgCl_2$, 2mM EGTA) to remove free Cy3. Typical labeling efficiencies were 20-30%. Cy3 labeling for PIFE in Fig 2-1B, C, and E proceeded as above with the following exceptions, a 1:2 protein:dye ratio in SEC buffer was used and only a single desalting step followed labeling. For head to head FRET, labeling with Alexa Fluor 488 C_5 Maleimide and Alexa Fluor 647 C_2 Maleimide (Thermo Fisher Scientific) proceeded as above with two desalting steps, except the S270C construct described above for FRET assays was used in place of the G343C construct, and the incubation time with dye was reduced to 30min. Typical labeling efficiencies were 50-70%.

PIFE assays. For GMPPNP PIFE kinetics (Fig 2-3), cytoDATL labeled with Cy3 was mixed with 1mM nucleotide (final) using a stopped flow accessory mounted on a PTI QuantaMaster-400 fluorometer (Horiba Instruments Inc., Edison, NJ) and 570nm fluorescence was monitored at 1sec intervals after

540nm excitation. Data was acquired using the FelixGX software (Horiba Instruments Inc., Edison, NJ) and normalized using the following equation: (Fluorescence – Minimum fluorescence observed) / (Maximum fluorescence observed – Minimum fluorescence observed). All data shown represent the average of 3 runs/mutant variant. PIFE data in Fig 2-1B, C, and E were captured using a Tecan M1000 (Tecan Group Ltd., Switzerland) and either a single representative trace (Fig 2-1B,C) or the average of 3 runs (Fig 2-1E) is shown. For GTP kinetics (Fig 2-1D, Fig 2-2C,D), cytoDATL labeled with Cy3 was mixed with GTP in a stopped flow device (Applied Photophysics SX20, Beverly, MA). Cy3 was excited at 540nm and the resulting change in fluorescence emission was observed with a 560nm long pass filter at 2.5msec intervals. Plotted data were the average of 7 runs/mutant variant. Data were normalized as described above and all PIFE data was replicated with similar results from at least two independent protein preps. All PIFE assays were carried out at 25°C in SEC buffer with 2mM □-mercaptoethanol. All data analysis was in Microsoft Excel (Redmond, WA).

FRET Assays. Head to head dimerization kinetics were monitored by adapting a FRET assay previously described for atlastin1 (Byrnes et al., 2013). CytoDATL labeled (as described above) with Alexa488 (donor) and Alexa647 (acceptor) at a 1:2 donor to acceptor ratio (1µM total cytoDATL final) was mixed with 1mM nucleotide (final). GMPPNP kinetics used the stopped flow attachment on the PTI-QuantaMaster400 fluorometer (described above) with a second emission monochromator. Following mixing with GMPPNP the donor (in the presence or absence of acceptor) was excited at 490nm and both donor and acceptor fluorescence emission monitored at 1sec intervals at 520 and 670nm, respectively. Due to lowered instrument noise in the donor channel, FRET efficiency (E) was calculated from the donor signal using the equation: $E = 1 – (I_{DA}/I_D)$ where I_{DA} is the donor intensity in presence of acceptor and I_D is donor intensity in absence of acceptor. FRET efficiency across mutant variants was normalized in the same way as the PIFE data and all traces represent the average of 3 runs/mutant variant. GTP

kinetics used the stopped flow device (described above). Following mixing with GTP the donor was excited at 470nm and donor fluorescence emission monitored with a 520/30 bandpass filter at 2.5msec intervals. As above, FRET efficiency was calculated from the donor signal. For GTP kinetics, the data shown represent the average of at least 7 runs/mutant variant. Crossover FRET kinetics with GTP was monitored by adapting a previously described assay for hATL1 (Byrnes et al., 2013). CytoDATL-mCer3 and cytoDATL-SYFP at a 1:2 donor to acceptor ratio was mixed with GTP in the stopped flow device. Donor was excited at 433nm and donor fluorescence emission in the presence or absence of acceptor was monitored with a 480/40nm bandpass filter at 2.5msec intervals. At least 7 runs were averaged. FRET efficiency was calculated and the data normalized as above. All assays were carried out in SEC buffer + 2mM β-mercaptoethanol at 25°C. All FRET data was replicated with similar results from at least two independent protein preps. All data analysis was in Microsoft Excel (Redmond, WA).

For measurement of crossover dimer stability, a modified form of a previously described assay was used (Liu et al., 2015). 2µM total Alexa488 and Alexa647 labeled DATL (1:1 donor:acceptor) was incubated at 28°C for 10 minutes in a Tecan Safire2 plate reader and a baseline of acceptor fluorescence was taken by excitation of the donor at 490nm and measuring acceptor emission at 670nm. Following this, 1mM GMPPNP was added and allowed to incubate for 1 hour at 28°C. After confirming a plateau in the FRET signal, a 5-fold molar excess of the corresponding unlabeled cytoDATL variant or buffer (50µl added to a reaction volume of 200µl) was added to the reaction mixture and acceptor fluorescence was monitored at 1sec intervals for 2h. Data were normalized using the following equation: (Fluorescence - minimum) / (Maximum - minimum) where minimum was the initial baseline and maximum was the starting value just after the unlabeled cytoDATL was added. Each trace is the average of 3 experimental replicates. Apparent k values were calculated by fitting the above averaged data to a double exponential curve. Of the two components to the fit the small amplitude (<0.12) faster (t1/2<60s) component was present in

all mutant variants with similar kinetics to the buffer control and assumed not to reflect the atlastin off rate. The reported k values are for the slower, larger amplitude, component that varied by mutant variant. The k values for wild type and K320M were assumed to be zero as little or no signal loss was observed over 2h over buffer alone. All assays were carried out in SEC buffer with 2mM □-mercaptoethanol.

Proteoliposome production and fusion Assay. Lipids in chloroform dried down by rotary evaporation were hydrated by resuspension in A100 buffer (25mM HEPES, pH 7.4, 100mM KCl, 10% glycerol, 2mM 2-mercaptoethanol, 1mM EDTA containing 5mM $MgCl_2$) at a final lipid concentration ~10mM and subjected to 12 freeze-thaw cycles in liquid N2 and room temperature (RT) water. Liposomes (100-300nm diameter) were formed by extrusion through 100nm polycarbonate filters using the LipoFast LF-50 extruder (Avestin, Ottawa, ON, Canada) and checked for size by dynamic light scattering (Zen3600, Malvern, UK). Full length DATL was inserted at a 1:1000 ratio of protein:lipid into labeled and unlabeled populations of liposomes at an effective detergent-to-lipid ratio of ~0.7 by incubating protein and lipid at 4°C for 1h followed by detergent removal by SM-2 Bio-Beads (Bio-Rad, Hercules, CA) at 1g beads per 70mg Anapoe X-100. Insoluble protein aggregates were pelleted by centrifugation of the samples in a microcentrifuge for 10min at 16,000xg. Thereafter reconstituted proteoliposomes were adjusted to 50% Nycodenz and separated from unincorporated protein by flotation through a (50%/45%/0%) Nycodenz (Axis-Shield, Dundee, Scotland) 5ml step gradient made in A100 buffer without glycerol. After centrifugation at 40,000rpm for 16h at 4°C in a SW50.1 rotor (Beckman Coulter), the gradient was fractionated and analyzed by SDS-PAGE to assess insertion efficiency. Finally, the floated fraction was desalted over a 2.4ml Sephadex A (GE Healthcare) column into A100 buffer, stored at 4°C and used

within 72h (Moss et al., 2011; Saini et al., 2014). Unlabeled vesicles consisted of 1-palmitoyl-2-oleoyl-sn-glycero-3- phosphocholine (PC) and 1,2-dioleoyl-sn-glycero-3-phospho-L-serine (PS) at an 85:15 ratio. Labeled vesicles consisted of PC, PS, Marina Blue 1,2-Dihexadecanoyl-*sn*-Glycero-3-Phosphoethanolamine (MB), 1,3- dipalmitoyl-sn-glycero-3-phosphoethanolamine-N-(7-nitro-2-1,3-benzoxadiazol-4-yl) (NBD) at an 82:15:1.5:1.5 ratio. For the fusion assay, proteoliposomes (0.6mM total lipid) were incubated in A100 buffer at a 1:2 ratio of labeled:unlabeled proteoliposomes. Following a 10 minute incubation at 37°C, 2mM GTP was added to the proteoliposome mixture and fluorescence de-quenching of MB was monitored every 30 seconds for one hour by exciting at 370nm and measuring the emission at 465nm using a Tecan M1000 plate reader. Following this 0.5% Anapoe X-100 was added to the mixture to disrupt the liposomes for determination of the maximal possible de-quenching. Data were plotted using the following equation: (Fluorescence – minimum) / (Maximum – minimum) and the average of three runs was graphed.

Tethering assay. Tethering activity was monitored using labeled vesicles with full-length DATL inserted at a 1:1000 protein:lipid ratio (0.6mM total lipid) in A100 buffer containing 5mM $MgCl_2$ as in the fusion assay described above. Following a 10 minute incubation at 37°C, 2mM GTP or an equivalent amount of buffer was added and the absorbance of each reaction was monitored at 405nm every 30s for one hour in a Tecan M1000. For each run, the absorbance of the proteoliposomes without GTP was subtracted from the absorbance with GTP, and the average of 3 runs was graphed.

GTPase assay. GTPase activity was measured as previously described (Hackney and Jiang, 2001) using a continuous coupled assay in which the hydrolysis product GDP serves as co-substrate in a reaction catalyzed by pyruvate kinase: PEP + GDP -> pyruvate + GTP. The pyruvate in turn is reduced by lactate

dehydrogenase in a reaction coupled to the oxidative loss of NADH (to NAD^+), which is measured as 340nm absorbance in a spectrophotometer. Each assay contained 2mM PEP, 0.1mg/ml pyruvate kinase, 0.15mM NADH, 6µg/ml lactate dehydrogenase in 200µl SEC buffer. After pre-incubation at 25°C with the indicated concentrations of cytoDATL, Mg-GTP was added to 1mM and NADH absorbance at 340nm monitored over time at 25°C to obtain the reaction rate for three independent measurements, which was subsequently divided by the cytoDATL concentration to obtain k_{obs}. Each data point represents the average of 3 replicates.

Crosslinking. The crosslinking assay was as previously described, except modified to greatly shorten the crosslinking time (Saini et al., 2014). 2µM atlastin was mixed with 1mM GMPPNP in SEC buffer at room temperature to initiate the crossover reaction. Following either an incubation time of 1min or 1h, the reaction mixture was diluted 1:1 with 100µM cross-linker (50µM final), either bismaleimidoethane (BMOE) or MTS-17-O5-MTS (MTS-17). After 20sec the reaction was quenched by diluting 1:1 with 50mM 1,4-Dithiothreitol (DTT) for BMOE or 20mM *N*-Ethylmaleimide (NEM) for MTS-17 (25mM or 10mM final, respectively). The cross-linked samples were then resolved by SDS-PAGE to determine the level of crosslinking. The data shown are representative of at least two independent experiments.

Online supplemental material

Fig 2-S1 shows that all cytoDATL variants have similar steady state GTPase activity. Fig 2-S2 shows that normalization does not alter PIFE kinetics. Fig 2-S3 shows the range of ER morphological changes in response to expression of the most severely destabilized crossover mutant variants K320G and P317G Venus-DATL. Fig 2-S4 shows a similar extent of incorporation of each DATL mutant variant into proteoliposomes.

Acknowledgements

M. Bruchez and J. Minden (Carnegie Mellon University, Pittsburgh, PA) shared instruments; M. Bruchez gave helpful advice on the fluorescence assays; C. Telmer (Carnegie Mellon University) provided mCer3 and SYFP; S. Saini and A. Linstedt (Carnegie Mellon University) provided helpful comments on the manuscript; and anonymous reviewers made important suggestions that improved the study. This work was funded by a grant to T.H.L. from the National Institutes of Health (NIH R01GM107285) and supplement (NIH R01GM107285-02S1).

Author contributions

J.W. and T.H.L. designed and carried out the experiments, J.W., D.D.H. and T.H.L. analyzed the data and T.H.L. and J.W. wrote the manuscript.

The authors declare no competing financial interests.

References

Bian, X., R.W. Klemm, T.Y. Liu, M. Zhang, S. Sun, X. Sui, X. Liu, T.A. Rapoport, and J. Hu. 2011. Structures of the atlastin GTPase provide insight into homotypic fusion of endoplasmic reticulum membranes. *Proc Natl Acad Sci U S A*. 108:3976-3981.

Byrnes, L.J., A. Singh, K. Szeto, N.M. Benvin, J.P. O'Donnell, W.R. Zipfel, and H. Sondermann. 2013. Structural basis for conformational switching and GTP loading of the large G protein atlastin. *EMBO J*. 32:369-384.

Byrnes, L.J., and H. Sondermann. 2011. Structural basis for the nucleotide-dependent dimerization of the large G protein atlastin-1/SPG3A. *Proc Natl Acad Sci U S A*. 108:2216-2221.

Carr, C.M., C. Chaudhry, and P.S. Kim. 1997. Influenza hemagglutinin is spring-loaded by a metastable native conformation. *Proc Natl Acad Sci U S A*. 94:14306-14313.

Chen, Y.A., and R.H. Scheller. 2001. SNARE-mediated membrane fusion. *Nat Rev Mol Cell Biol*. 2:98-106.

Cohen, F.S., and G.B. Melikyan. 2004. The energetics of membrane fusion from binding, through hemifusion, pore formation, and pore enlargement. *J Membr Biol*. 199:1-14.

Daumke, O., and G.J. Praefcke. 2011. Structural insights into membrane fusion at the endoplasmic reticulum. *Proc Natl Acad Sci U S A*. 108:2175-2176.

Eckert, D.M., and P.S. Kim. 2001. Mechanisms of viral membrane fusion and its inhibition. *Annu Rev Biochem*. 70:777-810.

Fasshauer, D., W. Antonin, V. Subramaniam, and R. Jahn. 2002. SNARE assembly and disassembly exhibit a pronounced hysteresis. *Nat Struct Biol*. 9:144-151.

Faust, J.E., T. Desai, A. Verma, I. Ulengin, T.L. Sun, T.J. Moss, M.A. Betancourt, H.W. Huang, T. Lee, and J.A. McNew. 2015. The Atlastin C-terminal Tail is an Amphipathic Helix that Perturbs Bilayer Structure during Endoplasmic Reticulum Homotypic Fusion. *J Biol Chem*.

Frolov, V.A., and J. Zimmerberg. 2010. Cooperative elastic stresses, the hydrophobic effect, and lipid tilt in membrane remodeling. *FEBS Lett*. 584:1824-1829.

Gao, Y., S. Zorman, G. Gundersen, Z. Xi, L. Ma, G. Sirinakis, J.E. Rothman, and Y. Zhang. 2012. Single reconstituted neuronal SNARE complexes zipper in three distinct stages. *Science*. 337:1340-1343.

Ghosh, A., G.J. Praefcke, L. Renault, A. Wittinghofer, and C. Herrmann. 2006. How guanylate-binding proteins achieve assembly-stimulated processive cleavage of GTP to GMP. *Nature*. 440:101-104.

Gruber, H.J., C.D. Hahn, G. Kada, C.K. Riener, G.S. Harms, W. Ahrer, T.G. Dax, and H.G. Knaus. 2000. Anomalous fluorescence enhancement of Cy3 and cy3.5 versus anomalous fluorescence loss of Cy5 and Cy7 upon covalent linking to IgG and noncovalent binding to avidin. *Bioconjug Chem*. 11:696-704.

Hackney, D.D., and W. Jiang. 2001. Assays for kinesin microtubule-stimulated ATPase activity. *Methods Mol Biol*. 164:65-71.

Hwang, H., H. Kim, and S. Myong. Protein induced fluorescence enhancement as a single molecule assay with short distance sensitivity. *Proc Natl Acad Sci U S A*. 108:7414-7418.

Jahn, R., and R.H. Scheller. 2006. SNAREs--engines for membrane fusion. *Nat Rev Mol Cell Biol*. 7:631-643.

Kozlov, M.M., H.T. McMahon, and L.V. Chernomordik. 2010. Protein-driven membrane stresses in fusion and fission. *Trends Biochem Sci*. 35:699-706.

Kuzmin, P.I., J. Zimmerberg, Y.A. Chizmadzhev, and F.S. Cohen. 2001. A quantitative model for membrane fusion based on low-energy intermediates. *Proc Natl Acad Sci U S A*. 98:7235-7240.

Li, F., F. Pincet, E. Perez, W.S. Eng, T.J. Melia, J.E. Rothman, and D. Tareste. 2007. Energetics and dynamics of SNAREpin folding across lipid bilayers. *Nat Struct Mol Biol*. 14:890-896.

Liu, T.Y., X. Bian, F.B. Romano, T. Shemesh, T.A. Rapoport, and J. Hu. 2015. Cis and trans interactions between atlastin molecules during membrane fusion. *Proc Natl Acad Sci U S A*. 112:E1851-1860.

Liu, T.Y., X. Bian, S. Sun, X. Hu, R.W. Klemm, W.A. Prinz, T.A. Rapoport, and J. Hu. 2012. Lipid interaction of the C terminus and association of the transmembrane segments facilitate atlastin-mediated homotypic endoplasmic reticulum fusion. *Proc Natl Acad Sci U S A*. 109:E2146-2154.

Liu, W., V. Montana, J. Bai, E.R. Chapman, U. Mohideen, and V. Parpura. 2006. Single molecule mechanical probing of the SNARE protein interactions. *Biophys J*. 91:744-758.

Loo, T.W., and D.M. Clarke. 2001. Determining the dimensions of the drug-binding domain of human P-glycoprotein using thiol cross-linking compounds as molecular rulers. *J Biol Chem*. 276:36877-36880.

Markin, V.S., and J.P. Albanesi. 2002. Membrane fusion: stalk model revisited. *Biophys J*. 82:693-712.

McNew, J.A., H. Sondermann, T. Lee, M. Stern, and F. Brandizzi. 2013. GTP-Dependent Membrane Fusion. *Annu Rev Cell Dev Biol*.

Morin-Leisk, J., S.G. Saini, X. Meng, A.M. Makhov, P. Zhang, and T.H. Lee. 2011. An intramolecular salt bridge drives the soluble domain of GTP-bound atlastin into the postfusion conformation. *J Cell Biol*. 195:605-615.

Moss, T.J., C. Andreazza, A. Verma, A. Daga, and J.A. McNew. 2011. Membrane fusion by the GTPase atlastin requires a conserved C-terminal cytoplasmic tail and dimerization through the middle domain. *Proc Natl Acad Sci U S A*. 108:11133-11138.

Mujumdar, R.B., L.A. Ernst, S.R. Mujumdar, C.J. Lewis, and A.S. Waggoner. 1993. Cyanine dye labeling reagents: sulfoindocyanine succinimidyl esters. *Bioconjug Chem*. 4:105-111.

Orso, G., D. Pendin, S. Liu, J. Tosetto, T.J. Moss, J.E. Faust, M. Micaroni, A. Egorova, A. Martinuzzi, J.A. McNew, and A. Daga. 2009. Homotypic fusion of ER membranes requires the dynamin-like GTPase atlastin. *Nature*. 460:978-983.

Park, S.H., and C. Blackstone. 2010. Further assembly required: construction and dynamics of the endoplasmic reticulum network. *EMBO Rep*. 11:515-521.

Saini, S.G., C. Liu, P. Zhang, and T.H. Lee. 2014. Membrane tethering by the atlastin GTPase depends on GTP hydrolysis but not on forming the crossover configuration. *Mol Biol Cell*.

Skehel, J.J., and D.C. Wiley. 2000. Receptor binding and membrane fusion in virus entry: the influenza hemagglutinin. *Annu Rev Biochem*. 69:531-569.

Sollner, T.H. 2004. Intracellular and viral membrane fusion: a uniting mechanism. *Curr Opin Cell Biol*. 16:429-435.

Stein, A., G. Weber, M.C. Wahl, and R. Jahn. 2009. Helical extension of the neuronal SNARE complex into the membrane. *Nature*. 460:525-528.

Sutton, R.B., D. Fasshauer, R. Jahn, and A.T. Brunger. 1998. Crystal structure of a SNARE complex involved in synaptic exocytosis at 2.4 A resolution. *Nature*. 395:347-353.

Südhof, T.C., and J.E. Rothman. 2009. Membrane fusion: grappling with SNARE and SM proteins. *Science*. 323:474-477.

Tamm, L.K. 2003. Hypothesis: spring-loaded boomerang mechanism of influenza hemagglutinin-mediated membrane fusion. *Biochim Biophys Acta*. 1614:14-23.

Tamm, L.K., J. Crane, and V. Kiessling. 2003. Membrane fusion: a structural perspective on the interplay of lipids and proteins. *Curr Opin Struct Biol*. 13:453-466.

Weissenhorn, W., A. Carfí, K.H. Lee, J.J. Skehel, and D.C. Wiley. 1998. Crystal structure of the Ebola virus membrane fusion subunit, GP2, from the envelope glycoprotein ectodomain. *Mol Cell*. 2:605-616.

Weissenhorn, W., A. Dessen, L.J. Calder, S.C. Harrison, J.J. Skehel, and D.C. Wiley. 1999. Structural basis for membrane fusion by enveloped viruses. *Mol Membr Biol*. 16:3-9.

Weissenhorn, W., A. Hinz, and Y. Gaudin. 2007. Virus membrane fusion. *FEBS Lett*. 581:2150-2155.

Yersin, A., H. Hirling, P. Steiner, S. Magnin, R. Regazzi, B. Hüni, P. Huguenot, P. De los Rios, G. Dietler, S. Catsicas, and S. Kasas. 2003. Interactions between synaptic vesicle fusion proteins explored by atomic force microscopy. *Proc Natl Acad Sci U S A*. 100:8736-8741.

Zhao, X., D. Alvarado, S. Rainier, R. Lemons, P. Hedera, C.H. Weber, T. Tukel, M. Apak, T. Heiman-Patterson, L. Ming, M. Bui, and J.K. Fink. 2001. Mutations in a newly identified GTPase gene cause autosomal dominant hereditary spastic paraplegia. *Nat Genet*. 29:326-331.

GTP hydrolysis drives disassembly of the atlastin crossover dimer

James Winsor, Ursula Machi, Qixiu Han, David D Hackney and Tina H Lee

Department of Biological Sciences, Carnegie Mellon University

4400 5th Avenue, Pittsburgh, PA 15213

- This article is in preparation for submission

Abstract

Homotypic endoplasmic reticulum membrane fusion is catalyzed when atlastin GTPases anchored in opposing membranes dimerize and undergo a crossed over conformational rearrangement that draws the bilayers together (Hu and Rapoport, 2016; McNew et al., 2013). Dimerization and crossover are delayed and fusion is inhibited when GTP hydrolysis is hindered, either through the use of non-hydrolysable GTP analogs, or by mutation of a key catalytic arginine residue to alanine (R48A/R77A) (Byrnes et al., 2013; Liu et al., 2015; Orso et al., 2009; Pendin et al., 2011; Saini et al., 2014; Winsor et al., 2017). This has led to current models in which GTP hydrolysis triggers dimerization and crossover, thus directly driving fusion. Here, we make the surprising observation that wild type (WT) atlastin undergoes dimerization and crossover prior to hydrolyzing GTP, and that nucleotide hydrolysis and Pi release closely coincide with dimer disassembly; thus indicating that hydrolysis cannot be the driver of crossover dimerization. In an effort to reconcile these findings with earlier observations, we screened for additional catalytic mutations that could be used to independently evaluate the role of GTP hydrolysis. Our screen revealed a new atlastin mutation that profoundly slows GTP hydrolysis but produces initial kinetics of dimerization and fusion similar to the WT. This suggests that GTP binding, rather than hydrolysis, triggers dimerization and fusion. It also confirms a structure-based prediction that the previously used arginine mutation exerts a direct effect on dimerization. Finally, we explain the inability of the non-hydrolysable GTP analog GMPPNP to trigger fusion by showing that it is incapable of inducing a G domain conformational change rapidly induced upon GTP binding. Together, these data indicate that GTP binding produces an atlastin conformation that strongly favors crossover dimer formation for lipid mixing, and that subsequent hydrolysis of GTP serves to recycle the protein for additional rounds of fusion. Thus, the atlastin mechanism unexpectedly parallels the SNARE fusion paradigm (Jahn and Scheller, 2006; Sollner, 2004), in which an energetically downhill formation of a stable protein complex drives fusion (Sutton et al., 1998; Weber et al., 1998; Winsor et al., 2017), followed by an input of energy

from nucleotide hydrolysis driving complex disassembly for subunit recycling (Otto et al., 1997; Zhao and Brunger, 2016).

Main

The soluble domain of human atlastin1 (hATL1) or Drosophila atlastin (*D*ATL), truncated to remove the trans-membrane domain and cytoplasmic tail, is induced to undergo crossover dimer formation by either GTP or its non-hydrolysable analogs (Byrnes et al., 2013; Byrnes and Sondermann, 2011; Liu et al., 2015; Moss et al., 2011; O'Donnell et al., 2017; Winsor et al., 2017; Wu et al., 2015). However, GTP triggers dimerization and crossover 100-fold more rapidly than either GMPPNP or GTPγS (Byrnes et al., 2013; O'Donnell et al., 2017; Winsor et al., 2017). This key observation has led to models in which atlastin monomers might associate with one another in the GTP-bound state, but GTP hydrolysis is required to stabilize the dimer interface for crossover (Byrnes et al., 2013; Liu et al., 2015; Saini et al., 2014; Winsor et al., 2017). A more recent report has gone further, suggesting that the hydrolysis of nucleotide occurs prior to dimerization and that the role of hydrolysis is to produce a GDP•Pi bound conformational state within the monomer that then triggers dimerization (O'Donnell et al., 2017). Both models predict fast GTP hydrolysis that either precedes, or is concurrent with dimerization, and then release of inorganic phosphate (Pi), leading to dimer disassembly.

Previous kinetic assays of the soluble domain of hATL1 (cyt-hATL1) or *D*ATL (cyt-*D*ATL) have used excess GTP (Byrnes et al., 2013; Liu et al., 2015; O'Donnell et al., 2017; Winsor et al., 2017), which permits multiple rounds of dimer assembly and disassembly, obscuring the timing and sequence of later events such as disassembly and Pi release. Here, we used a sub-stoichiometric GTP concentration to limit the reaction to just one round of dimer formation and disassembly. To examine the rate of crossover dimer assembly and disassembly, we used our previously established Protein Induced Fluorescence Enhancement (PIFE) assay (Winsor et al., 2017). This assay places an environmentally sensitive fluorophore Cy3 on the three-helix bundle of cyt-*D*ATL. Upon crossover, the fluorescence of the dye is enhanced as it becomes buried at the three-helix bundle dimer interface rather than being exposed to solvent (Fig 3-1a). Our previous assays used G343C on the three-helix bundle of cyt-*D*ATL as

the labeling site; however, that site also detected an early and transient conformational shift likely related to the release of the three-helix bundle from the G domain prior to crossover (Winsor et al., 2017). By moving the labeling site 10Å further down the three-helix bundle and away from the G domain, we eliminated the initial deflection while retaining the same sensitivity to crossover. As expected (Byrnes et al., 2013), the previously studied hydrolysis defective R48A Cy3-labeled cyt-*D*ATL showed only a negligible PIFE signal at early times after mixing with GTP (Fig 3-1b). In contrast, the WT underwent rapid crossover dimer formation, followed by disassembly, resulting in a complete return to the monomer state by 30sec (Fig 3-1b). Interestingly, the end state had a lower fluorescence than the initial nucleotide-free monomer, likely due to a difference in the positioning of the three-helix bundle in the GDP-bound monomer (Bian et al., 2011; Byrnes et al., 2013; Byrnes and Sondermann, 2011). Previous studies have shown G domain dimerization to coincide with, or slightly precede, crossover formation (O'Donnell et al., 2017; Winsor et al., 2017). To ensure that this was the case under the single turnover condition used here, we independently monitored G domain, or head to head (H/H), dimerization using cyt-*D*ATL labeled with FRET donor and acceptor fluorophores on an engineered G domain residue S270C (Fig 3-1c), as done previously (Byrnes et al., 2013; O'Donnell et al., 2017; Winsor et al., 2017). As anticipated (O'Donnell et al., 2017; Winsor et al., 2017), the two traces were nearly identical, with H/H dimerization possibly just preceding crossover (Fig 3-1d).

Based on the recently reported GTP hydrolysis burst rate constant of $27sec^{-1}$ for cyt-hATL1 (O'Donnell et al., 2017), we anticipated that the hydrolysis of GTP by cyt-*D*ATL under the single turnover condition used here would be well completed by 1-2s. In contrast to this expectation, we observed incomplete hydrolysis, even after 10s (Fig 3-1e). The approximate turnover time of ~20s for hydrolysis observed here contrasts sharply with the recently reported burst rate but is consistent with earlier steady state turnover numbers of ~$3min^{-1}$ for cyt-*D*ATL (Orso et al., 2009; Saini et al., 2014) (and also below). Given previously reported GTP binding affinities and on and off rates (Byrnes et al., 2013), this

over 500-fold difference in burst rate is difficult to attribute entirely to slowed nucleotide binding due to the lower GTP concentration in our assay. The discrepancy may be due to the saturating level of GTP used previously (O'Donnell et al., 2017), which may have made it difficult to separate a burst phase from the steady state, and which may also have resulted in a high background of GDP and Pi. In any case, the discrepancy was not due to a difference between hATL1 and *D*ATL because each showed similar hydrolysis rates using sub-stoichiometric GTP (Fig 3-1f compared to Fig 3-1e).

Most surprisingly, overlaying the averaged hydrolysis data (from Fig 3-1e and additional replicates) onto the PIFE trace of crossover revealed that crossover dimer formation precedes the hydrolysis of nucleotide by a significant margin (Fig 3-1g). This unexpected observation contradicted all previous models, including our own, in which nucleotide hydrolysis either stabilizes the dimer interface or creates a dimerization competent conformation. Instead, the timing of GTP hydrolysis coincided more closely with that of dimer disassembly. We also measured Pi release using *E coli* phosphate binding protein (PBP) (Kubena et al., 1986) labeled with the fluorescent coumarin derivative, MDCC, to produce the Pi sensor, MDCC-PBP (Brune et al., 1994). Pi binding is rapid (k_{on}>100$\mu M^{-1}s^{-1}$) and high affinity (K_D~0.1μM), and has been established to cause a conformational change in MDCC-PBP that increases its fluorescence intensity (Brune et al., 1994). In our assay, Pi release closely coincided with GTP hydrolysis (Fig 3-1g). The absence of a discernable lag between hydrolysis and Pi release implies that Pi release is fast and limited only by the rate of hydrolysis. Overall, these kinetic data suggested that dimerization and crossover both precede GTP hydrolysis; and hydrolysis, occuring more slowly, is rapidly followed by Pi release to trigger the disassembly of the atlastin crossover dimer.

These observations contradicted earlier data obtained using the R48A *D*ATL mutation (R77A in hATL1) to inhibit GTP hydrolysis. We, as well as others, had previously observed the R48A mutation to block both tethering and fusion (Pendin et al., 2011; Saini et al., 2014) and to greatly slow crossover dimer formation (Byrnes et al., 2013) (see also Fig 3-1b), implying a requirement for hydrolysis in dimer

formation, tethering and fusion. Importantly however, while the R48 residue performs a crucial role in catalyzing GTP hydrolysis (Pendin et al., 2011), the equivalent R77 residue in hATL1 is at the G domain dimer interface in one of the three hATL1 dimer crystal structures (Bian et al., 2011; Byrnes and Sondermann, 2011), implying that this residue may also play a role in dimerization. In human guanylate binding protein1 (hGBP1), a GTPase closely related to atlastin (Zhao et al., 2001), the equivalent arginine residue undergoes rearrangement during dimerization, moving from the dimer interface towards the active site to facilitate nucleotide hydrolysis (Ghosh et al., 2006). Therefore, we suspected that the R48A mutation in *D*ATL might cause a dimerization defect separate from its hydrolysis defect. This is especially likely as the GTP-induced dimerization of cyt-hATL1 (R77A) has been observed to be noticeably slower than GMPPNP-induced dimerization of WT cyt-hATL1 (Byrnes et al., 2013), something unexpected if a lack of hydrolysis were the only defect in both cases.

To re-evaluate the role of hydrolysis in dimer formation, we set out to identify a new mutation whose sole effect might be on nucleotide hydrolysis. For screening purposes, we took advantage of existing structural and biochemical data on hGBP1 (Ghosh et al., 2006). In hGBP1, a switch 1 serine residue, S73 (Fig 3-2a), interacts with the water nucleophile in the GDP•AlF_4 transition state crystal structure (Fig 3-2b) and its mutation to alanine inhibits nucleotide hydrolysis (Ghosh et al., 2006). This serine residue is not conserved in the switch 1 region of either hATL1 or *D*ATL (Fig 3-2a, S73 highlighted in blue). However, S73 in hGBP1 is also within hydrogen bonding distance to an aspartate residue D103 in switch 2 (Fig 3-2b). The latter aspartate residue is not only conserved in both hATL1 and *D*ATL (Fig 3-2a, also highlighted in blue), but the corresponding residue in hATL1 (D152 in hATL1 and D127 in *D*ATL) additionally contacts a water molecule that may assist in catalysis (Fig 3-2b). Targeting this conserved aspartate residue D127, as well as the non-conserved S73 equivalent residue R93, for mutagenesis, we found either a D127N or D127A substitution in cyt-*D*ATL to abolish steady state GTP hydrolysis (Fig 3-2c). In comparison, an R93A substitution had no effect and R93Q had a modest effect (Fig 3-2c). Notably,

neither D127 nor R93 (D152 and R118 in hATL1) is at the dimer interface in any of the hATL1 crystal structures (Bian et al., 2011; Byrnes et al., 2013; Byrnes and Sondermann, 2011), making them less likely to be involved directly in dimerization. Of the two D127 substitutions that blocked steady state GTP hydrolysis (Fig 3-2c), we chose D127N for further analysis as it reflected a more conservative substitution; however, similar results have been obtained with D127A.

To assess the dimerization and crossover properties of D127N cyt-*D*ATL, we first looked at its crossover PIFE kinetics under conditions of excess GTP. Here, D127N cyt-*D*ATL showed a GTP induced crossover kinetic that was ~3-fold slower than the WT but remarkably robust nevertheless (Fig 3-2d). The relatively rapid dimerization and crossover by D127N, in spite of its apparent inability to hydrolyze GTP (Fig 3-2c), further reinforced our previous results that crossover formation is not coupled directly to GTP hydrolysis. It also confirmed that the slow rate of dimerization and crossover seen previously with R48A (Byrnes et al., 2013) was most likely the result of a dimerization defect separate from hydrolysis. Additionally, crossover of D127N cyt-*D*ATL was profoundly slowed when GTP was substituted with GMPPNP, just as for the WT (Byrnes et al., 2013; Winsor et al., 2017) (Fig 3-2e). The substantial difference in D127N crossover rate with GMPPNP relative to GTP even in the absence of hydrolysis further suggested that GMPPNP is likely an imperfect mimic of GTP in the atlastin system (see below).

Although our steady state assay of GTP hydrolysis suggested a complete block to hydrolysis for D127N cyt-*D*ATL (Fig 3-2c), our single turnover assay revealed a low level of hydrolysis activity. However, the hydrolysis activity of D127N was extremely slow in comparison to WT (Fig 3-3a). Whereas WT cyt-*D*ATL hydrolyzed nucleotide to near completion by 10-20 seconds after GTP addition (see also Fig 3-1e and 1g), D127N cyt-*D*ATL required 20-40 minutes to complete a single round (Fig 3-3a). This kinetic block to hydrolysis provided an ideal platform to test whether the hydrolysis of GTP might be the trigger for dimer disassembly. As anticipated, dimerization and crossover by D127N cyt-*D*ATL was rapid even under the single turnover condition, with crossover formation largely completed by 30sec (Fig 3-3b), a time

when the hydrolysis of GTP by this variant had just begun (Fig 3-3a). The D127N disassembly kinetic, by contrast, was profoundly slowed as compared to WT (Fig 3-3b), and was incomplete even after 30min (Fig 3-3c). Notably, the time to complete disassembly was on par with the time to complete hydrolysis (Fig 3-3c and Fig 3-3a), in agreement with a role for GTP hydrolysis in triggering dimer disassembly. Also, as observed for WT, Pi release by D127N cyt-*D*ATL coincided well with nucleotide hydrolysis (Fig 3-3c) again implying that GTP hydrolysis is rate limiting for Pi release.

The robust crossover kinetics of D127N, along with our observation that GTP hydrolysis primarily impacts disassembly, a step believed to occur post membrane fusion, led us to predict that fusion by D127N may be initially unimpeded. If so, we also predicted that subsequent cycles might be disrupted due to the slow rate of dimer disassembly and subunit recycling by this variant. To test this, we looked at the membrane fusion capability of D127N versus R48A and WT in the presence or absence of saturating GTP. We incorporated full-length versions of each *D*ATL variant into synthetic vesicles and used a standard lipid-mixing assay to determine the relative rates of fusion. As expected from previous reports (Pendin et al., 2011), R48A showed no fusion activity at all, while WT showed robust GTP dependent activity (Fig 3-3d). Remarkably, and consistent with the lack of a major dimerization defect, D127N *D*ATL catalyzed GTP dependent fusion at a rate that was similar to the WT, at least at early times (Fig 3-3e). Thus neither crossover formation nor fusion appears to require prior hydrolysis of GTP. At later times, the lipid-mixing activity by D127N ceased (Fig 3-3d), consistent with our prediction that the inability to undergo dimer disassembly would prevent the recycling of D127N atlastin subunits required for multiple rounds of fusion catalysis.

The ability of atlastin to initiate crossover formation and fusion well before hydrolysis supported the idea that GTP binding, rather than its hydrolysis, is the primary driver of dimerization and fusion. However, this idea was contradicted by the long-standing observation that *D*ATL is completely inert in a fusion assay when GTP is replaced by either GMPPNP or GTP□S (Orso et al., 2009; Saini et al., 2014). On

the other hand, the yeast ATL-like protein Sey1p has been reported to have a low level of fusion activity with GMPPNP (Yan et al., 2015). The different behavior of Sey1p could be due to its more extended three-helix bundle rendering the molecule more permissive for crossing over (Yan et al., 2015); alternatively it could be due to a difference within its G domain. As both molecules are capable of binding GMPPNP (Byrnes et al., 2013; Yan et al., 2015), we reasoned that the active sites of the two proteins might differ to the extent that GMPPNP bound to Sey1p, but not *D*ATL, is capable of producing the conformation change necessary to trigger rapid dimerization. If this were the case, a *D*ATL G domain conformational change should be observable upon binding GTP but not GMPPNP. To test this, we used intrinsic tryptophan fluorescence, which utilizes the sensitivity of tryptophan to its environment to monitor protein conformational change in a label-free system (Ghisaidoobe and Chung, 2014). The soluble domain of *D*ATL contains four tryptophan residues all restricted to the G domain, making it likely that upon nucleotide binding one or more will experience changes in its environment that will result in an observable fluorescence change.

As anticipated, tryptophan fluorescence emission by WT cyt-*D*ATL showed a striking drop within the first 100ms of mixing with GTP but not with either buffer or GDP, indicating a clear GTP induced G domain conformational change (Fig 3-4a). To ensure that the rapid fluorescence change observed upon GTP addition was not caused by dimerization or crossover, we also monitored crossover dimerization by PIFE. Under the same condition, the PIFE kinetic was clearly much slower, confirming that the tryptophan fluorescence change reflects a conformation change distinct from dimerization or crossover (Fig 3-4b). The G domain change depended on GTP concentration with a half maximal concentration ~10μM GTP (Fig 3-4c), consistent with previously reported GTP affinities for hATL1 using mant-labeled nucleotides (Byrnes et al., 2013). Strikingly, while those previous reports indicated that GMPPNP binds cyt-hATL1 with an affinity similar to GDP or GTP (Byrnes et al., 2013), cyt-*D*ATL tryptophan fluorescence emission showed no significant change upon addition of GMPPNP (Fig 3-4a). Thus cyt-*D*ATL is either

unable to adopt the GTP induced conformation upon GMPPNP binding, or the conformational change is much slower. In either case, GTP binding rapidly induces a unique G domain conformation that GMPPNP is unable to completely replicate. We presume that this conformational change strongly favors dimerization and crossover for fusion. Furthermore, testing D127N cyto-*D*ATL under the same conditions yielded similar results to the WT (Fig 3-4d), indicating that the observed conformation change is hydrolysis independent and results solely from GTP binding. R48A cyto-*D*ATL also showed a conformation change upon GTP addition (Fig 3-4e); however, the magnitude of the fluorescence change was reduced compared to WT and D127N, perhaps indicating an incomplete or different conformational shift upon nucleotide binding. Altogether, these data indicate that GTP binding on its own induces a conformational change in the atlastin G domain that renders rapid crossover dimer formation and initiation of lipid-mixing an energetically downhill reaction; and the nucleotide analog GMPPNP is incapable of triggering this change. Subsequent to fusion, GTP hydrolysis and the rapid release of Pi return atlastin to a conformation that strongly favors the monomer state; thus enabling the recycling of atlastin subunits for reuse.

The initial discovery of the atlastin GTPase as a membrane fusion catalyst (Bian et al., 2011; Byrnes and Sondermann, 2011; Orso et al., 2009) naturally raised the question of whether its mechanism of fusion would bear any resemblance to that of previously studied fusion catalysts. We recently showed that formation of the atlastin crossover dimer energizes fusion (Winsor et al., 2017) in a manner analogous to coiled coil bundle formation energizing SNARE dependent fusion (Jahn and Scheller, 2006; Weber et al., 1998). Our findings here extend that analogy and demonstrate just how conceptually similar the atlastin fusion mechanism is to the SNARE mechanism, the main difference being that whereas SNAREs rely on the ATPase NSF for subunit recycling after fusion (Jahn and Scheller, 2006; Otto et al., 1997; Zhao and Brunger, 2016), the recycling mechanism for atlastin is built into the fusion apparatus. For atlastin, the same dimer formation reaction that drives membrane fusion appears to also

trigger nucleotide hydrolysis, leading to rapid dimer disassembly following fusion. Notably, the picture of the atlastin reaction cycle emerging from this study also bears resemblance to other G proteins activated by dimerization (GADs) (Gasper et al., 2009), for whom GTP binding induced dimerization triggers both the biological function of the GTPase and nucleotide hydrolysis induced dimer disassembly to initiate a new reaction cycle (Gasper et al., 2009). An analysis of the evolutionary history of atlastin and other GADs such as the SRP and SRP receptor (Shan et al., 2007) has revealed that they are the products of an early split in the diversification of P-loop NTPases (Leipe et al., 2002; Shan, 2016). Therefore, the general mechanism of activation of G proteins by GTP-dependent dimerization and inactivation upon nucleotide hydrolysis appears to have evolved multiple times during evolution to regulate a wide variety of biological processes.

Figures

Figure 1. Atlastin crossover dimer formation precedes GTP hydrolysis and Pi release.

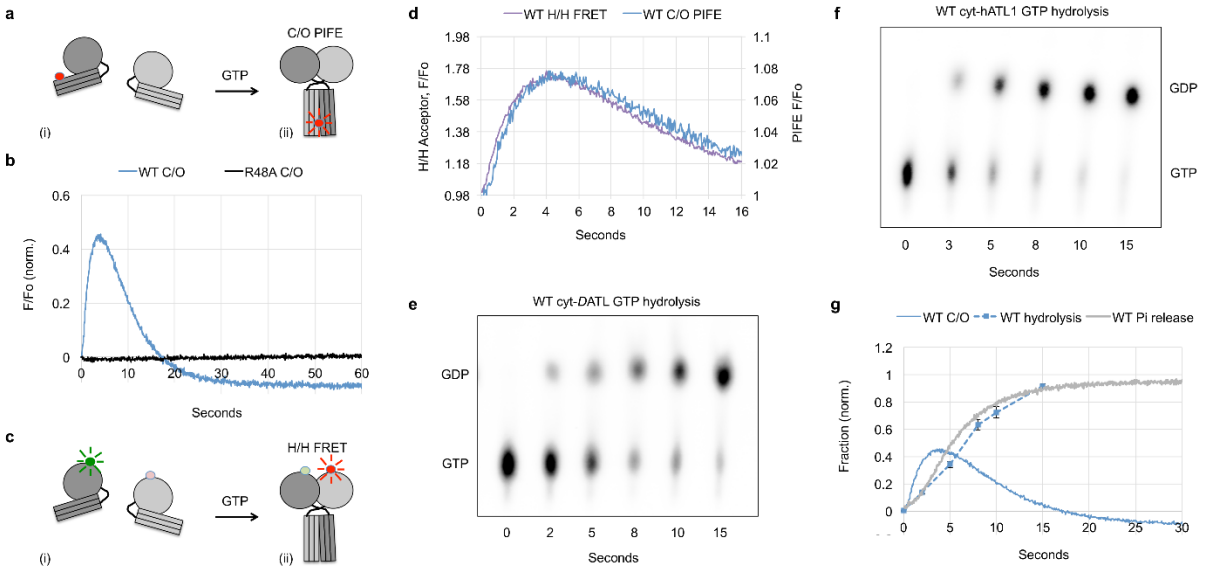

Figure 3-1. Atlastin crossover dimer formation precedes GTP hydrolysis and Pi release. a-g, Single turnover kinetics. All reactions contained 15µM cyt-DATL and 7.5µM GTP (final concentrations) and were carried out at 25°C except where indicated. **a**, Schematic of Cy3 fluorescence enhancement (PIFE) as a Cy3-labeled cyt-*D*ATL (i) undergoes dimer formation and crossover (ii). **b**, Stopped flow PIFE of WT or R48A after addition of GTP. **c**, Schematic of FRET as cyt-*D*ATL monomers labeled with a FRET donor and acceptor (i) undergo head to head (H/H) dimerization (ii). **d**, Comparison of stopped flow WT head to head FRET (H/H) with WT crossover PIFE (C/O). **e**, GTP hydrolysis after incubation of WT cyt-*D*ATL with GTP (containing a-^{32}P-GTP) at room temperature. Reactions were quenched at the indicated times (1 of 3 replicates shown). **f**, The same assay as in **e** carried out with WT cyt-hATL1. **g**, Comparison of WT crossover PIFE (C/O), GTP hydrolysis and Pi release. PIFE (C/O) trace is from **b**. GTP hydrolysis was the average of 3 replicates from **e** (+/-s.e.m.). Pi release was measured by including 15µM MDCC-PBP (final) in the stopped flow. All traces were normalized to the maximum possible signal in each assay and all traces are the average of 3-5 individual traces and representative of 2 independent protein preparations.

Figure 2. The D127N catalytic mutation inhibits GTP hydrolysis but not crossover dimer formation.

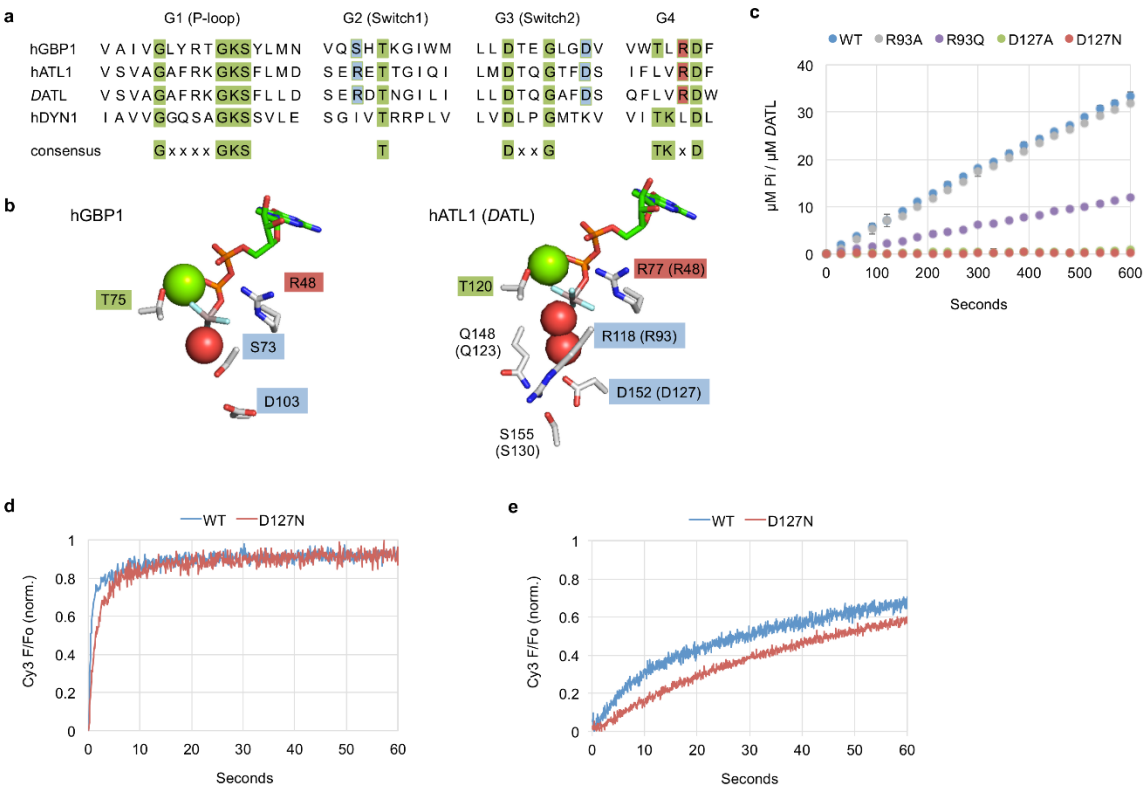

Figure 3-2. The D127N catalytic mutation inhibits GTP hydrolysis but not crossover dimer formation. a, Sequence alignment of hGBP1, hATL1, *D*ATL and human dynamin1 (hDYN1) showing the positions of D127 and R93 in *D*ATL relative to other signature GTPase residues. Residues conserved across GTPases in green, catalytic arginine in red and D127 and R93 in blue. **b**, Side chains of active site residues in hGBP1 (PDB 2B92) and hATL1 (PDB 4IDQ) bound to GDP•AlF_4 rendered in PyMOL. Magnesium ion and waters as green and red spheres, respectively. **c**, Steady state GTPase assay measuring Pi release by WT, D127A, D127N, R93A and R93Q cyt-*D*ATL upon addition of GTP (n=3, +/-s.e.m.). **d**, Stopped flow PIFE of WT or D127N cyt-*D*ATL after addition of excess GTP. **e**, Stopped flow PIFE of WT or D127N cyt-*D*ATL after addition of excess GMPPNP. Stopped flow traces (**d,e**) are the average of 3 runs, normalized to the maximum possible signal and representative of two independent protein preparations.

Figure 3. GTP hydrolysis is not required for crossover formation or initial fusion.

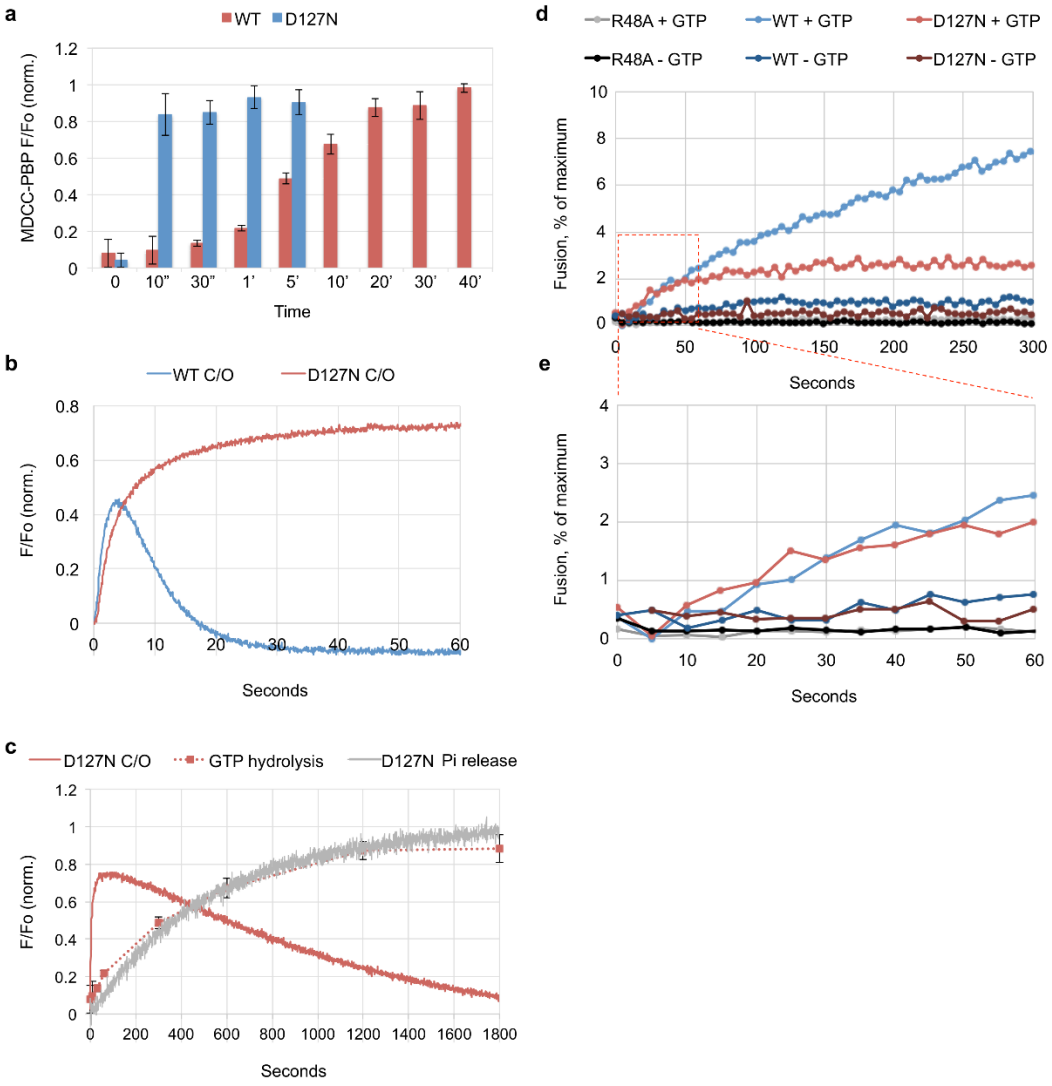

Figure 3-3. GTP hydrolysis is not required for crossover formation or initial fusion. a-c, WT and D127N single turnover kinetics. All reactions contained 15µM cyt-*D*ATL and 7.5µM GTP (final concentrations) and were carried out at 25°C except where indicated. **a**, GTP hydrolysis by WT or D127N cyt-*D*ATL at room temperature. Reactions were quenched at the indicated times and total Pi produced measured after 10 fold dilution into 1.5µM MDCC-PBP (n=3, +/-S.D). **b**, Stopped flow PIFE of WT or D127N cyt-*D*ATL after addition of GTP. Fluorescence was normalized to the maximum PIFE signal obtained after mixing with saturating GTP. The WT trace is the same as in Fig 1b. **c**, Comparison of D127N crossover PIFE (C/O), GTP hydrolysis and Pi release. GTP hydrolysis was re-plotted from **a**. D127N Pi release was measured as in Fig 1g. **d,** Full-length WT, R48A or D127N *D*ATL was reconstituted into donor and acceptor vesicles at a 1:1000 protein:lipid ratio and fusion monitored as the de-quenching of NBD-labeled lipid present in the donor vesicles over time at 28°C after addition of 1mM GTP (average of 3 runs plotted). **e**, Magnified view of the early time points of traces boxed in **d**. Stopped flow, GTP hydrolysis and fusion kinetics are all representative of two independent protein preparations.

Figure 4. GMPPNP does not replicate the GTP-induced G domain conformation change.

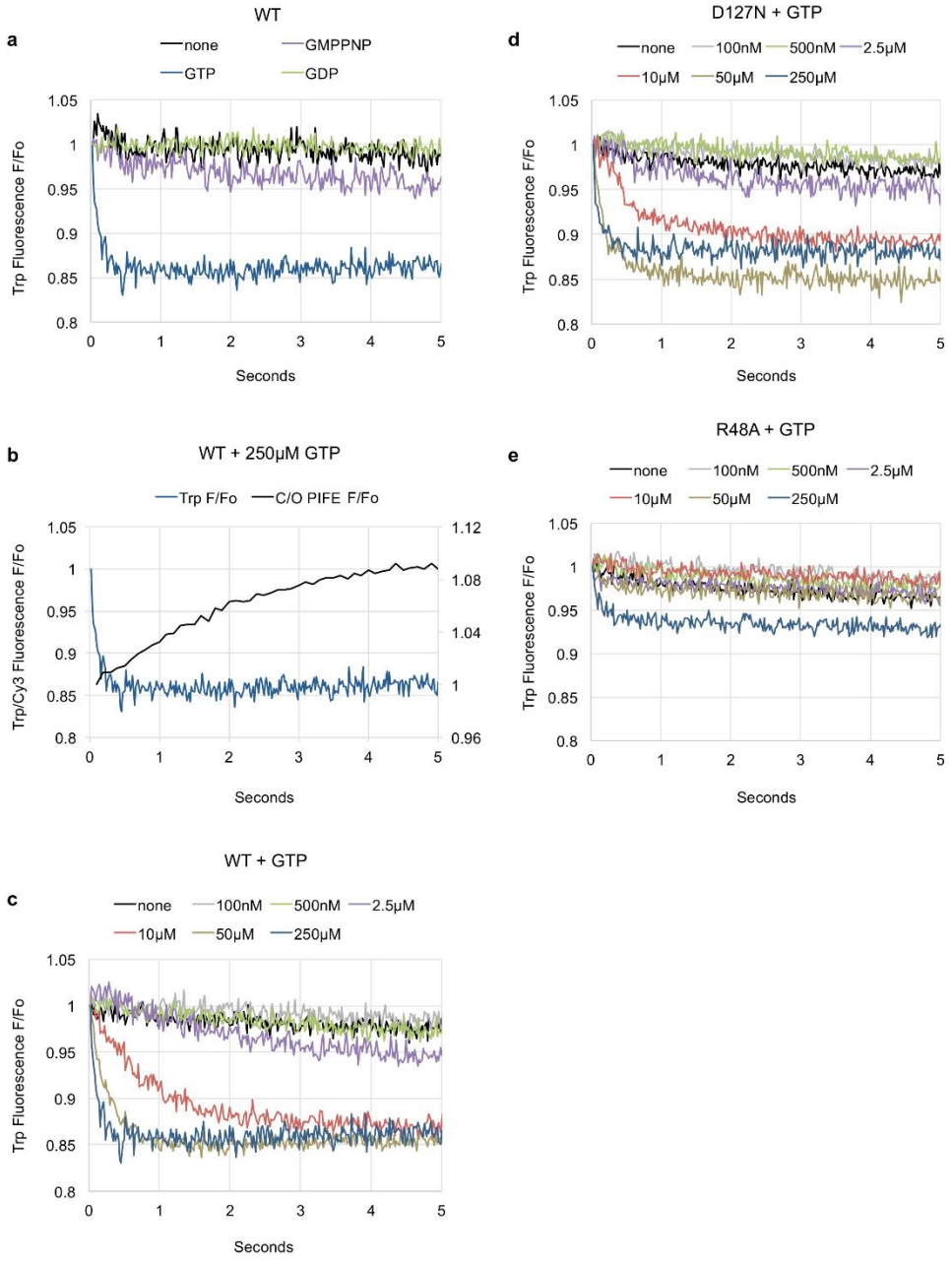

Figure 3-4. GMPPNP does not replicate the GTP-induced G domain conformation change. a-e, Intrinsic tryptophan fluorescence of 125nM WT, D127N or R48A cyt-*D*ATL after addition of the indicated concentrations of the indicated nucleotides at 25°C. **a**, WT after mixing with 250µM GTP, GDP, GMPPNP or buffer. **b**, GTP induced tryptophan fluorescence quenching is much more rapid than crossover dimerization under the same conditions. WT tryptophan fluorescence trace with 250µM GTP (from **a**) re-plotted relative to crossover PIFE under the same conditions. **c**, WT tryptophan fluorescence quenching with the indicated concentrations of GTP. **d**, D127N with the indicated concentrations of GTP. **e**, R48A with the indicated concentrations of GTP. All concentrations are final after mixing.

Methods

Reagents and constructs. The soluble domain cyt-*D*ATL construct was 6xHis-tagged at the N-terminus by cloning AA1-415 of *D*ATL into NheI and EcoRI sites of the pRSETB vector as before (Saini et al., 2014; Winsor et al., 2017), except that it had an engineered cysteine at H410C for the PIFE assays. The soluble domain of hATL1 (AA1-446) was similarly 6xHis-tagged at the N-terminus. The full-length *D*ATL 'WT' parent construct, also 6xHis-tagged at the N-terminus using the same cloning strategy, had the following cysteine substitutions: G343C, C429L, C452L, C501A, C350A as before (Saini et al., 2014; Winsor et al., 2017). The cysteine-substituted full-length protein was previously shown to have fusion activity similar to the WT (Saini et al., 2014). All amino acid substituted constructs were generated using PCR mutagenesis and fully sequence confirmed (GENEWIZ, South Plainfield, NJ). Nucleotides were purchased from Sigma-Aldrich (Burlington, MA), reconstituted to 100mM stocks in 10mM Tris pH 8.0, 1mM EDTA and stored at -80°C. Lipids were purchased from Avanti Polar Lipids (Alabaster, AL).

Protein expression and purification. Expression of cyt-*D*ATL was in (DE3) pLysS *E. coli* grown at 25°C to OD~0.6 and induced with 0.5mM isopropyl □-D-1-thiogalactopyranoside (IPTG) overnight at 20°C. Cells were harvested, washed once with cold PBS and flash frozen. All purification steps were conducted on ice or at 4°C with chilled buffers. Cell pellets (from 2L of culture) were resuspended in 20ml lysis buffer (50mM Tris pH 8.0, 5mM $MgCl_2$, 10mM imidazole, 500mM NaCl, 10% glycerol, 0.5mM PMSF, 1µg/ml pepstatin, 1µM leupeptin, 2mM 2-mercaptoethanol (2-ME)) per liter of culture and sonicated 4x 5 minutes, 50% duty cycle, output control setting #3 with a microtip on a Branson sonifier 250 (Branson Ultrasonics, Danbury, CT) with 5 minute rests between rounds. Samples were then spun at 10,500rpm in a SA600 rotor (Sorvall, Thermo Fisher Scientific) for 30 minutes, and the supernatant spun at 50,000rpm in a Ti70 rotor (Beckman Coulter, Indianapolis, IN) for 1 hour. The final supernatant was mixed with 0.25ml Ni-NTA agarose (Qiagen, Hilden, Germany) for 2 hours, poured into a column support and

washed with 30mL of wash buffer (50mM Tris pH 8.0, 5mM $MgCl_2$, 20mM imidazole, 100mM NaCl, 10% glycerol, 2mM 2-ME). Protein was eluted in 0.25ml fractions with elution buffer (50mM Tris pH 8.0, 5mM $MgCl_2$, 250mM imidazole, 100mM NaCl, 10% glycerol, and 2mM 2-ME). Fractions were flash frozen and stored at -80°C. Samples of each fraction were resolved by SDS-PAGE and determined to be >95% pure. Expression of full-length *D*ATL was also in (DE3)pLysS *E. coli* grown at 25°C but induced at OD~0.4 with 0.2mM IPTG at 18°C for 2.5 hours. Harvesting was as above and all purification steps were on ice or at 4°C. Cell pellets (from 4L of culture) were resuspended in 10mL lysis buffer containing 4% Triton X-100 (Sigma-Aldrich) per liter of culture, sonicated and cleared of insoluble material as above. The final supernatant was diluted to 1% Tx-100 using lysis buffer and then loaded (from the bottom) overnight onto a pre-poured 0.5ml Ni-NTA agarose column. The following day the column was washed with 30mL of lysis buffer with 1% Triton X-100, then with 30mL of wash buffer with 0.1% Anapoe X-100 (Affymetrix, Santa Clara, CA). The protein was eluted in 0.5ml fractions with elution buffer containing 0.1% Anapoe X-100. Fractions were flash frozen and stored at -80°C. Samples of each fraction were resolved by SDS-PAGE and determined to be ≥50% pure.

Steady state GTPase assay. GTPase activity of cyt-*D*ATL was measured under steady state conditions (Fig 3-2c) using the EnzChek Phosphate Assay Kit (Molecular Probes, Thermo Fisher Scientific, Waltham, MA) on a TECAN Safire2 plate reader (Tecan, Zurich, Switzerland). Purified cyt-*D*ATL protein was desalted into SEC buffer (25mM Tris-HCl pH 7.5, 100mM NaCl, 2mM EGTA, 5mM $MgCl_2$, 2mM 2-ME) without magnesium. A standard reaction involved mixing 1U/ml purine nucleoside phosphorylase (PNP), 0.2 mM 2-amino-6-mercapto-7-methylpurine riboside (MESG), 2µM cyt-*D*ATL and 0.5 mM GTP in 50 mM Tris-HCl pH 7.5, 100 mM NaCl, 2mM 2-ME, in a total volume of 0.2ml at 28°C. The reaction was started with the addition of 5mM $MgCl_2$. Therefore buffers provided within the EnzCheck kit were altered so that they did not contain any magnesium.

MDCC-PBP purification. MDCC-PBP was prepared following a previously published protocol (Solscheid et al., 2015). Expression from the plasmid PstS1 encoding PBP A197C (Addgene, Cambridge, MA) was in (DE3) pLysS *E. coli* grown at 37°C to OD~0.8 and induced with 0.5mM IPTG for 4h at 37°C. Cells were harvested, washed twice in cold 10mM Tris pH 8.0 and 30mM NaCl, resuspended in 20mM Tris pH 8.0 (20ml per 500ml culture) and flash frozen. All purification steps were on ice or at 4°C. Cells (from 0.5L of culture) were thawed with addition of 1mM DTT and 0.5mM PMSF, homogenized, sonicated 3x 0.5min, 50% duty cycle, #3 setting and cleared by low and high-speed centrifugation as above. The resulting supernatant was adjusted to have the same conductivity as buffer A (10mM Tris pH 8.0) and loaded onto a 5ml Q sepharose (GE Healthcare, Chicago, IL) column pre-equilibrated in buffer A. After washing with 30mls buffer A, protein was eluted in 2.5ml fractions with a 50ml gradient (0-200mM NaCl) in buffer A. Peak fractions were pooled, concentrated with a C-10 Amicon centriprep (Sigma-Aldrich), flash frozen and stored at -80°C. For MDCC labeling, 2-3 PBP preparations were pooled and dialyzed against 20mM Tris pH 8.0, 100µM EDTA and then placed in a 15ml Falcon tube to achieve 100µM PBP in a volume of 8mls and a Pi mop added (200µM MEG (Sigma-Aldrich), 0.2U/ml microbial PNPase (Sigma-Aldrich) final) at room temperature. After 5-10min, MDCC (Thermo Fisher Scientific) was added to 150µM from a DMSO stock, the tube wrapped in foil and rotated for 30min at room temperature. Precipitate was removed by centrifugation in a TLA100.3 (Beckman-Coulter) rotor, 100,000rpm, 10min, 4°C. The supernatant was adjusted to have the conductivity of Buffer A and the sample loaded onto a 20ml Q sepharose column equilibrated in buffer A. MDCC-PBP was eluted with a 400ml (0-50mM NaCl) gradient in buffer A in 4ml fractions. Peak fractions were concentrated to 1ml with a C-10 centriprep, flash frozen and stored at -80°C.

Single turnover GTPase assays. GTP hydrolysis activity under single turnover conditions (Fig 3-1e, f and Fig 3-3a) was measured using 15µM Cyt-*D*ATL and 7.5µM GTP in SEC buffer at room temperature. For the hydrolysis assay using radiolabeled GTP (Fig 3-1e, f), reactions had 15µM cyt-*D*ATL and 7.5µM GTP

(containing 1µCi/µl □-^{32}P-GTP (Perkin Elmer)) in SEC buffer at room temperature. At the indicated times, samples were quenched by addition of one volume of 1M perchloric acid, neutralized with addition of 0.75 volume of 1M KOAc and cleared by centrifugation at 4000rpm in a microcentrifuge for 2min to remove denatured protein. 3µl of each supernatant was loaded onto a PEI cellulose TLC plate (Machery-Nagel, Inc., Bethlehem, PA) and nucleotides resolved with a solution of 1M $LiCl_2$ and 1M formic acid for 2h. After drying, samples were visualized using a phoshporimager (Typhoon, Amersham, Waltham, MA). Alternately, for the hydrolysis assay using MDCC-PBP (Fig 3-3a), reactions were stopped at the indicated times by boiling for 2min and then cleared with a 2min, 16,000xg microcentrifuge spin. The supernatant of each reaction (20µl) was diluted 10-fold into SEC buffer containing MDCC-PBP to achieve a final concentration of 1.5µM MDCC-PBP. MDCC fluorescence was measured in a Tecan Safire2 plate reader at 465nm after excitation at 430nm. A Pi standard curve showed the assay to be linear with Pi concentration over the range of Pi produced under these conditions.

Cy3 labeling for PIFE and FRET. Cyt-*D*ATL containing an engineered cysteine at H410C was desalted over a 4ml Sephadex G-25 (Sigma-Aldrich) column pre-equilibrated with labeling buffer (25mM Tris pH 7.0, 100mM NaCl, 5mM $MgCl_2$, 2mM EGTA, 1mM imidazole, 500µM TCEP). Cy3 maleimide (GE Healthcare) was added from a DMSO stock at a 1:1 protein:dye molar ratio and incubated for 2h at room temperature before being centrifuged at 100,000rpm in a TLA100 rotor for 10min at 4°C to remove any precipitate. Labeled cyt-*D*ATL was then desalted twice as above to remove free Cy3. Typical labeling efficiencies were 20-30%. Differences in labeling efficiency did not alter the rate of crossover formation. Alexa Fluor 488/647 labeling for the FRET assay followed essentially the same procedure except that it used cyt-*D*ATL containing an engineered cysteine at S270C.

PIFE assays of crossover. For multiple turnover assays with either GTP or GMPPNP (Fig 3-2d and e), 2µM cyt-*D*ATL labeled with Cy3 as described above was mixed with 1mM nucleotide (final concentrations

after mixing) in SEC buffer at 25°C using a stopped flow accessory mounted on a PTI QuantaMaster-400 fluorometer (Horiba Instruments Inc., Edison, NJ) and 570nm fluorescence was monitored at 100ms intervals after 540nm excitation. Data was acquired using the FelixGX software (Horiba Instruments Inc.). After calculation of F/Fo for each run, the runs were averaged and then normalized using the equation (Fluorescence – Minimum fluorescence observed) / (Maximum fluorescence observed – Minimum fluorescence observed) where fluorescence is F/Fo. All data shown are the average of at least 3 runs per condition. All data analysis was in Microsoft Excel (Redmond, WA). Single turnover PIFE assays were essentially the same as above except that the final concentrations after mixing were 15µM cyt-*D*ATL and 7.5µM GTP in SEC buffer, data were acquired at 50ms intervals and all data shown are the average of 3 runs per condition after normalization to the maximum PIFE signal with saturating (1mM) GTP. Each of the 3 PIFE traces was nearly identical to the others and each result was reproduced with at least two independent protein preparations.

FRET assay for head to head dimerization. Head to head dimerization kinetics under single turnover conditions used cyt-*D*ATL (S270C) labeled with Alexa Fluor 488 (donor) and Alexa Fluor 647 (acceptor) mixed at a 1:2 donor/acceptor ratio (15µM total cyt-*D*ATL final) with 7.5µM GTP (final) in SEC buffer at 25°C. Measurements were acquired with the same equipment as for PIFE. Both donor and acceptor fluorescence emission with 490nm donor excitation was monitored at 50ms intervals at 520 and 670nm respectively, though only the acceptor emission trace is shown (Fig 3-1d). The data shown are the average F/Fo traces of 3 runs without normalization and each run was nearly identical to the others.

Pi release kinetics. Assay conditions followed the above for single turnover PIFE, except that unlabeled cyt-*D*ATL was mixed with MDCC-PBP prior to mixing with GTP so that the final concentrations after mixing were 15µM cyt-*D*ATL, 15µM MDCC-PBP and 7.5µM GTP in SEC buffer. MDCC fluorescence at 465nm was monitored at 50ms intervals at 25°C with 430nm excitation. All data shown are the average

of 3 runs per condition where each run was nearly identical to the others. Each result was reproduced with at least two independent protein preparations.

Tryptophan fluorescence quenching assay. 125nM unlabeled cyt-*D*ATL was mixed with various concentrations of nucleotide (all indicated concentrations were final after mixing) and tryptophan fluorescence monitored at 318nm every 20ms after excitation at 295nm. The fluorescence baseline for buffer at each nucleotide concentration without cyt-*D*ATL was subtracted from the fluorescence with cyt-*D*ATL prior to F/Fo calculations. Assays were carried out in SEC buffer at 25°C using stopped flow conditions as described above for PIFE. All data were the average of 3-5 traces.

Preparation of liposomes and lipid-mixing fusion assay. Lipids in chloroform dried down by rotary evaporation were hydrated by resuspension in A100 buffer (25mM HEPES pH 7.4, 100mM KCl, 10% glycerol, 1mM EDTA, 2mM 2-ME) at a final 10mM lipid concentration and subjected to 11 freeze-thaw cycles in liquid N_2 and 42°C water bath. Liposomes (100-300nm diameter) were formed by extrusion through 100nm polycarbonate filters using the LipoFast LF-50 extruder (Avestin, Ottawa, ON, Canada) and checked for size by dynamic light scattering (Zen3600, Malvern UK). Purified full-length *D*-ATL was incorporated at a 1:1000 protein:lipid ratio into labeled and unlabeled liposome populations at an effective detergent-to-lipid ratio of ~0.7 by incubating protein and lipid at 4°C for 1h followed by four detergent removal incubations by SM-2 Bio-Beads (Bio-Rad, Hercules, CA) at 1g beads per 70mg Anapoe X-100. Insoluble protein aggregates were pelleted by centrifugation in a microcentrifuge for 10min at 16,000xg. Thereafter reconstituted proteoliposomes were adjusted to 50% Nycodenz (Axis-Shield, Dundee, Scotland) and separated from unincorporated protein by flotation through a 5ml Nycodenz step gradient (50%/45%/0%) in A100 buffer without glycerol in a SW50.1 (Beckman-Coulter) rotor overnight. Finally, the floated fraction was desalted over a 2.4ml Sephadex G-25 column into A100 buffer, stored at 4°C and used within 72h or flash frozen and stored at -80°C. Unlabeled liposomes consisted of 1-palmitoyl-2-oleoyl-sn-glycero-3-phosphocholine (PC) and 1,2-dioleoyl-sn-glycero-3-

phospho-l-serine (PS) at an 85:15 ratio. Labeled liposomes consisted PC:PS:1,3- dipalmitoyl-*sn*-glycero-3-phosphoethanolamine-*N*-(7-nitro-2-1,3- benzoxadiazol-4-yl) (NBD):1,2-dipalmitoyl-*sn*-glycero-3-phosphoetha-nolamine-*N*-(lissamine rhodamine B sulfonyl) at an 82:15: 1.5:1.5 molar ratio. For the fusion assay, proteoliposomes (0.6mM total lipid) were incubated in A100 buffer containing 5mM $MgCl_2$ at a 1:3 ratio of labeled:unlabeled. Following a 10min incubation at 28°C in a Tecan M1000 plate reader, 2mM GTP was injected using the automated injector attachment and fluorescence de-quenching of NBD monitored at 5s intervals at 538nm after excitation at 460nm. After 10min, 0.5% Anapoe X-100 was added for determination of the maximum possible de-quenching signal. Data were plotted using the equation (Fluorescence observed – minimum fluorescence observed) / (Maximum fluorescence – minimum fluorescence) and the average of 3 runs is shown. The results were reproduced with at least two independent protein preparations and liposome incorporations.

Data availability statement. The datasets generated during and/or analyzed during the current study are available from the corresponding author on reasonable request.

Acknowledgements. We thank A. Linstedt for discussions throughout, G. Rule for suggestions on active site mutations, M. Webb (London, U.K.) for advice on producing MDCC-PBP, M. Bruchez and J. Minden for sharing equipment and A. Linstedt for critical comments on the manuscript. This work was supported by a grant from the National Institutes of Health/National Institute for General Medical Sciences R01GM107285 (to T.H.L.) and supplement R01GM107285-02S1.

Author contributions. J.W. performed the experiments and data analysis in Fig 3-1 and Fig 3-3b-c and Fig 3-4. U.M. performed the experiments and data analysis in Fig 3-2c-e and Fig 3-3d-e. T.H.L. performed the experiment and data analysis in Fig 3-3a. The initial screen identifying the D127N mutation was carried out by U.M. and Q.H. Modeling of the kinetic data was performed by D.D.H. The manuscript was written by T.H.L. and J.W.

Competing interests. The authors declare no competing interests.

Materials & correspondence. Correspondence and material requests should be addressed to Tina H Lee <thl@andrew.cmu.edu>.

References

Bian, X., R.W. Klemm, T.Y. Liu, M. Zhang, S. Sun, X. Sui, X. Liu, T.A. Rapoport, and J. Hu. 2011. Structures of the atlastin GTPase provide insight into homotypic fusion of endoplasmic reticulum membranes. *Proc Natl Acad Sci U S A*. 108:3976-3981.

Brune, M., J.L. Hunter, J.E. Corrie, and M.R. Webb. 1994. Direct, real-time measurement of rapid inorganic phosphate release using a novel fluorescent probe and its application to actomyosin subfragment 1 ATPase. *Biochemistry*. 33:8262-8271.

Byrnes, L.J., A. Singh, K. Szeto, N.M. Benvin, J.P. O'Donnell, W.R. Zipfel, and H. Sondermann. 2013. Structural basis for conformational switching and GTP loading of the large G protein atlastin. *EMBO J*. 32:369-384.

Byrnes, L.J., and H. Sondermann. 2011. Structural basis for the nucleotide-dependent dimerization of the large G protein atlastin-1/SPG3A. *Proc Natl Acad Sci U S A*. 108:2216-2221.

Gasper, R., S. Meyer, K. Gotthardt, M. Sirajuddin, and A. Wittinghofer. 2009. It takes two to tango: regulation of G proteins by dimerization. *Nat Rev Mol Cell Biol*. 10:423-429.

Ghisaidoobe, A.B., and S.J. Chung. 2014. Intrinsic tryptophan fluorescence in the detection and analysis of proteins: a focus on Förster resonance energy transfer techniques. *Int J Mol Sci*. 15:22518-22538.

Ghosh, A., G.J. Praefcke, L. Renault, A. Wittinghofer, and C. Herrmann. 2006. How guanylate-binding proteins achieve assembly-stimulated processive cleavage of GTP to GMP. *Nature*. 440:101-104.

Hu, J., and T.A. Rapoport. 2016. Fusion of the endoplasmic reticulum by membrane-bound GTPases. *Semin Cell Dev Biol*. 60:105-111.

Jahn, R., and R.H. Scheller. 2006. SNAREs--engines for membrane fusion. *Nat Rev Mol Cell Biol*. 7:631-643.

Kubena, B.D., H. Luecke, H. Rosenberg, and F.A. Quiocho. 1986. Crystallization and x-ray diffraction studies of a phosphate-binding protein involved in active transport in Escherichia coli. *J Biol Chem*. 261:7995-7996.

Leipe, D.D., Y.I. Wolf, E.V. Koonin, and L. Aravind. 2002. Classification and evolution of P-loop GTPases and related ATPases. *J Mol Biol*. 317:41-72.

Liu, T.Y., X. Bian, F.B. Romano, T. Shemesh, T.A. Rapoport, and J. Hu. 2015. Cis and trans interactions between atlastin molecules during membrane fusion. *Proc Natl Acad Sci U S A*. 112:E1851-1860.

McNew, J.A., H. Sondermann, T. Lee, M. Stern, and F. Brandizzi. 2013. GTP-Dependent Membrane Fusion. *Annu Rev Cell Dev Biol*.

Moss, T.J., C. Andreazza, A. Verma, A. Daga, and J.A. McNew. 2011. Membrane fusion by the GTPase atlastin requires a conserved C-terminal cytoplasmic tail and dimerization through the middle domain. *Proc Natl Acad Sci U S A*. 108:11133-11138.

O'Donnell, J.P., R.B. Cooley, C.M. Kelly, K. Miller, O.S. Andersen, R. Rusinova, and H. Sondermann. 2017. Timing and Reset Mechanism of GTP Hydrolysis-Driven Conformational Changes of Atlastin. *Structure*. 25:997-1010.e1014.

Orso, G., D. Pendin, S. Liu, J. Tosetto, T.J. Moss, J.E. Faust, M. Micaroni, A. Egorova, A. Martinuzzi, J.A. McNew, and A. Daga. 2009. Homotypic fusion of ER membranes requires the dynamin-like GTPase atlastin. *Nature*. 460:978-983.

Otto, H., P.I. Hanson, and R. Jahn. 1997. Assembly and disassembly of a ternary complex of synaptobrevin, syntaxin, and SNAP-25 in the membrane of synaptic vesicles. *Proc Natl Acad Sci U S A*. 94:6197-6201.

Pendin, D., J. Tosetto, T.J. Moss, C. Andreazza, S. Moro, J.A. McNew, and A. Daga. 2011. GTP-dependent packing of a three-helix bundle is required for atlastin-mediated fusion. *Proc Natl Acad Sci U S A*. 108:16283-16288.

Saini, S.G., C. Liu, P. Zhang, and T.H. Lee. 2014. Membrane tethering by the atlastin GTPase depends on GTP hydrolysis but not on forming the crossover configuration. *Mol Biol Cell*.

Shan, S.O. 2016. ATPase and GTPase Tangos Drive Intracellular Protein Transport. *Trends Biochem Sci*. 41:1050-1060.

Shan, S.O., S. Chandrasekar, and P. Walter. 2007. Conformational changes in the GTPase modules of the signal reception particle and its receptor drive initiation of protein translocation. *J Cell Biol*. 178:611-620.

Sollner, T.H. 2004. Intracellular and viral membrane fusion: a uniting mechanism. *Curr Opin Cell Biol*. 16:429-435.

Solscheid, C., S. Kunzelmann, C.T. Davis, J.L. Hunter, A. Nofer, and M.R. Webb. 2015. Development of a Reagentless Biosensor for Inorganic Phosphate, Applicable over a Wide Concentration Range. *Biochemistry*. 54:5054-5062.

Sutton, R.B., D. Fasshauer, R. Jahn, and A.T. Brunger. 1998. Crystal structure of a SNARE complex involved in synaptic exocytosis at 2.4 A resolution. *Nature*. 395:347-353.

Weber, T., B.V. Zemelman, J.A. McNew, B. Westermann, M. Gmachl, F. Parlati, T.H. Sollner, and J.E. Rothman. 1998. SNAREpins: minimal machinery for membrane fusion. *Cell*. 92:759-772.

Winsor, J., D.D. Hackney, and T.H. Lee. 2017. The crossover conformational shift of the GTPase atlastin provides the energy driving ER fusion. *J Cell Biol*. 216:1321-1335.

Wu, F., X. Hu, X. Bian, X. Liu, and J. Hu. 2015. Comparison of human and Drosophila atlastin GTPases. *Protein Cell*. 6:139-146.

Yan, L., S. Sun, W. Wang, J. Shi, X. Hu, S. Wang, D. Su, Z. Rao, J. Hu, and Z. Lou. 2015. Structures of the yeast dynamin-like GTPase Sey1p provide insight into homotypic ER fusion. *J Cell Biol*. 210:961-972.

Zhao, M., and A.T. Brunger. 2016. Recent Advances in Deciphering the Structure and Molecular Mechanism of the AAA+ ATPase N-Ethylmaleimide-Sensitive Factor (NSF). *J Mol Biol*. 428:1912-1926.

Zhao, X., D. Alvarado, S. Rainier, R. Lemons, P. Hedera, C.H. Weber, T. Tukel, M. Apak, T. Heiman-Patterson, L. Ming, M. Bui, and J.K. Fink. 2001. Mutations in a newly identified GTPase gene cause autosomal dominant hereditary spastic paraplegia. *Nat Genet*. 29:326-331.

Conclusion and Future Directions

While the broad outlines of atlastin's fusion mechanism seem clear there remain many open questions. This work has shown there is a clear distinction between the process influenced by crossover, fusion, versus hydrolysis, disassembly. This clear distinction should allow future work to provide accurate estimates of force generation through means such as optical tweezers. Accurate estimates of the energy released by atlastin crossover compared to known estimates of bilayer fusion requirements will allow an estimate of the number of atlastin fusion complexes required for membrane fusion. Most known fusion proteins operate through cooperative mechanisms due to the need for more energy than a single fusion complex can provide, and atlastin is implicated to be cooperative as well. The transmembrane region of atlastin has been suggested to act to mediate higher order interactions, however a mechanism for this action is not well understood. A better understanding of how many atlastin complexes must act in concert to trigger membrane fusion based on energetic measurements of crossover would be helpful to begin modeling how interactions may occur.

Further, nearly all kinetic data on atlastin other than fusion data to date has been collected using a truncated soluble domain constructs missing the transmembrane and C-terminal tail domains. This has proven to be fertile grounds for providing insights into the fusion mechanism, but viewing events such as dimerization and crossover in the context of full length atlastin may provide important insights. For example, in the soluble domain dimerization and crossover appear very nearly simultaneous. Does this hold true in the context of membranes, a context with substantial resistance present from the bilayers opposing crossover. Further, is crossover simultaneous with lipid mixing? It seems likely if crossover is providing the energy for fusion that they should be simultaneous, but has not been shown. Furthermore, SNARE proteins display a "zippering" mechanism where they can be arrested prior to fusion. It is not even known if atlastin's crossover proceeds as a single continuous step or if that is an artifact of the lack of resistance in the soluble domain. It is possible that when resistance is applied to

atlastin crossover may break apart into several smaller steps with their own energetic contributions. Direct observation of atlastin in membranes would be helpful to clear up these questions.

While this work did not touch upon the importance of the C-terminal tail of atlastin several open questions remain about it. It has been shown that the tail acts as an amphipathic helix that inserts into the lipid bilayer and that this is required for fusion. However, the amphipathic helix represents less than half of the total length of the conserved C-terminal helix present in all atlastins. Further, removal of the remainder of the helix results in a nearly 50% drop in fusion activity *in vitro*, a finding that remains completely unexplained. Even the mechanism of action by the amphipathic helix is unclear, it is proposed to disrupt bilayers during insertion as other helixes do, but other amphipathic helixes capable of disrupting bilayers are not sufficient to substitute for loss of atlastin's native helix.

Additionally, mutations to human atlastin-1, among other genes, result in the neurodegenerative conditions Hereditary Spastic Paraplegia (HSP) and Hereditary Sensory Neuropathy (HSN). Both diseases are a result of degeneration of long neurons that enervate the legs, however, the reason for this degeneration is not clear. Not all mutations associated with either disease result in any known phenotype when studied *in vitro* with Drosophila atlastin. Studying native atlastin-1 may be helpful in this case, however, to date, no known mammalian atlastin has been shown to be fusion competent. The reason for this may range from unknown accessory proteins being required in mammals to heterodimers between the different atlastins being required instead of homodimers as in invertebrates.